



A physically-based constitutive model for the shear-dominated response and strain rate effect of carbon fibre reinforced composites

Wei Tan^{a,c,*}, Burigede Liu^{b,c}

^a School of Engineering and Materials Science, Queen Mary University of London, London, E1 4NS, UK

^b Department of Mechanical and Civil Engineering, California Institute of Technology, Pasadena, CA, 91125, USA

^c Engineering Department, University of Cambridge, Cambridge, CB2 1PZ, UK

ARTICLE INFO

Keywords:

Polymer-matrix composites (PMCs)
Plastic deformation
Micro-mechanics
Computational modelling

ABSTRACT

A significant hardening response is often observed for the shear-dominated deformation of Carbon Fibre Reinforced Plastics (CFRP). This non-linear response is typically modelled by fitting a strain hardening law against experimental stress-strain curves. Inspired by crystal plasticity framework, we develop a micro-mechanically motivated constitutive model to capture the matrix shearing and fibre rotation of CFRP under finite strain deformation and different strain rates. Strain rate dependency of the shear modulus and yield strength of the matrix was modelled through scaling functions. This physically-based constitutive model is first verified by simple shear and transverse compression tests, followed by comprehensive validations against the measured stress-strain responses of unidirectional (UD) and cross-ply composite laminates subjected to quasi-static and dynamic off-axis loading. The finite element predictions and analytical models of CFRP lamina under simple shear loading confirms that the initial yielding is governed by the shear yield strength of matrix, while the hardening behaviour is dependent on the modulus and rotation of carbon fibres. This model accurately predicts the non-linear behaviour of CFRP under off-axis loading at different strain rates, without the need of a curve-fitted strain hardening law.

1. Introduction

Carbon Fibre Reinforced Plastics (CFRP) are finding increasing utilisation in lightweight transportation vehicles due to their high specific stiffness and strength. Under transverse or shear loading, the main response of a unidirectional (UD) CFRP is controlled by matrix, exhibiting large non-linear shear-dominated deformation and subsequent matrix cracking [1]. This non-linear hardening effect allows composite structures to bear loading under strain over 20%, which may create an additional safety margin to engineering structures [2,3]. It is therefore essential to understand the origin of non-linear stress strain responses of CFRP to determine design allowables for engineering composite structures. Shear-dominated behaviour has been observed in off-axis compression tests of unidirectional laminates [4], tensile or compressive loading on $\pm 45^\circ$ laminates [5–7] or V-notched rail shear tests on cross-ply laminates [1,8]. A significant amount of fibre rotation towards the loading axis can be observed in these composites [1,6]. Therefore, it is necessary to consider the fibre rotation and matrix yielding in a constitutive model in order to accurately predict the material response

under large deformations.

Models of composite laminates typically consist of a stress-strain constitutive model, a failure criterion to predict the material yielding and a damage evolution law that degrades the material modulus and sets the final failure state [9–11]. These models either assume a purely-elastic constitutive model or capture the non-linear behaviour by fitting the experimental stress-strain hardening law using master curves [1,7,12–16]. In order to account for the fibre rotation, models based on infinitesimal strain assumption [5,6,17,18] used a geometric relation between fibre rotation angle φ and local strains, ε_{xx} and ε_{yy} , by $\varphi = \arctan \frac{1+\varepsilon_{xx}}{1+\varepsilon_{yy}}$, which is only valid for the symmetrical $[\pm\theta]_{ns}$ composite laminates. Mandel et al. [19] proposed a constitutive model which includes two independent non-associative flow rules to describe yielding due to transverse and longitudinal shear loading, based on the finite deformation theory. The fibre rotation was accounted via a geometric equation. Vogler and Koerber et al. [20,21] modelled the non-linear behaviour by an elastic-viscoplastic constitutive model using invariant terms. Yield functions were defined, based on stress invariants, that

* Corresponding author. School of Engineering and Materials Science, Queen Mary University of London, London, E1 4NS, UK.

E-mail address: wei.tan@qmul.ac.uk (W. Tan).

<https://doi.org/10.1016/j.compositesb.2020.108032>

Received 27 July 2019; Received in revised form 31 March 2020; Accepted 1 April 2020

Available online 8 April 2020

1359-8368/© 2020 Elsevier Ltd. All rights reserved.

remain unchanged for arbitrary coordinate system transformations with respect to the fibre direction. This ensures the independent determination of material yielding regardless of fibre rotation. Laux [22] developed a non-associative plasticity model based on the invariants of transverse isotropy for the non-linear behaviour of UD composite materials.

A more general description of the anisotropic non-linear plastic deformation was developed by introducing the ‘plastic spin’ effect within Hill’s plasticity model [23]. Dafalias [24] modelled fibre rotation via a ‘plastic spin’ to describe the rotation of the material substructure (fibres) with respect to the overall material rotation. This involves additional tensorial constitutive rules for plastic spin based on the assumption that the material symmetries are invariant to plastic deformation. A similar strategy has recently been adopted by other researchers [25,26] to update the fibre rotation in the deformed configuration.

Crystal plasticity model originally developed for metals are also able to capture the material anisotropy and the texture evolution [27,28]. It assumes the plastic flow through the bulk metallic material is due to shearing along certain slip systems and plastic slip deformation does not alter the initial crystal orientation. Therefore, the ‘plastic spin’ effect is automatically considered within the crystal plasticity framework. Constitutive model based on crystal plasticity framework has been developed by Liu et al. [29–31] to model the ultra-high molecular weight polyethylene (UHMWPE) fibre composites. It was found that the deformation of the UHMWPE fibres is purely elastic and thus shearing of the matrix is restricted along certain slip planes dictated by the fibre directions. The model resembling the crystallographic slips is valid for UHMWPE composites since the yield strength of polyurethane matrices used for those composites is extremely low of 2 MPa. It was not clear if constitutive models based on similar concepts can be applied to CFRP which has a significantly stronger matrix with shear yield strength of more than 35 MPa. Recently, Meza et al. [32] have successfully employed this crystal plasticity model to capture the strain hardening effect of the 3D non-woven carbon fibre reinforced composites. However, the relation between fibre rotation and non-linear hardening behaviour was not explained analytically. The effect of slip systems and strain rates on the mechanical response has not been investigated yet.

Impact resistance and crashworthiness are the typical safety measures for CFRP used in the transportation vehicles. In the bird-strike or crash events of transport vehicles, strain rates of structural components are in the range of 100–1000/s. Experimental results found that both the moduli and strengths of CFRP varied with the strain rate [33]. To accurately assess the impact tolerance of composite structures, it is important to consider the strain rate effect in their constitutive models [33–37].

The strain rate dependency of the elastic moduli, non-linear shear behaviour and the strength properties was mostly introduced by fitting the available rate-dependent experimental data with scaling functions [38–40]. These models typically scale the material properties with known macroscopic strain rate at the beginning of numerical simulation. However, the local strain rate varies with position and time within the material particularly when plastic shear deformation is present [4]. Assuming a constant strain rate within the material may ignore the local rate-dependent shear deformation, hence affecting the accuracy of prediction. Strain rate effect is believed to be dominated by the polymer matrix, as measured in tensile tests of bulk epoxy matrix samples [5] and off-axis compressive tests of unidirectional laminates [4,39]. Therefore, a rate-dependent framework updating the yield strength of composite laminates based on its local strain rate is proposed in this model.

The purpose of the present study is to develop a physically-based constitutive model for composite laminates under finite deformation, and to predict its macroscopic mechanical behaviour under large matrix shearing and associated fibre rotation at different strain rates. A rate-dependent framework based on crystal plasticity was developed for composite laminates. We model each UD lamina as a homogenised solid

using the developed constitutive model which quantifies matrix shearing and fibre rotation under a finite deformation setting. The origin of non-linear hardening response is revealed through analytical and finite element models. The fidelity of the physically-based model is validated by comparing numerical results with the measured stress-strain responses of UD and cross-ply composite laminates subjected to off-axis loadings of various strain rates.

2. Physically-based model

To develop a micro-mechanically motivated constitutive model for CFRP composites, accurately capturing the fibre rotation and the strain rate effect, we shall proceed with a brief discussion of the deformation mechanisms of CFRP composite subjected to shear loading.

2.1. Experimental observations

The pure shear tests of unidirectional composite laminates conducted by Tan et al. [1] have shown that shear deformation is mainly achieved by the shearing of the matrix along the fibre direction, without fibre rotation, when shear loading is applied parallel to the fibre direction. Based on these experimental observations, we postulate that plastic shear deformation of the CFRP composites is predominantly the result of matrix shearing along certain slip directions dictated by the fibres. A direct consequence of this assumption is that under simple shear loading along fibre direction, the fibre rotation remains zero. It should be noted that this is in sharp contrast comparing to the assumption used by other classical constitutive models (e.g., Hill’s plasticity model [23]), where a

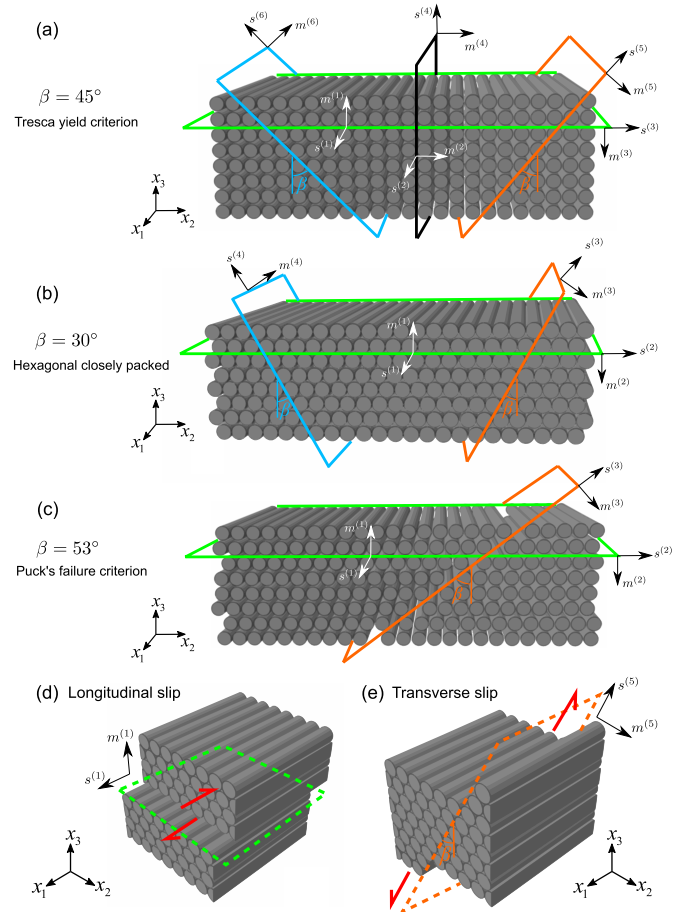


Fig. 1. Sketches of the full slip systems for (a) $\beta = 45^\circ$, (b) $\beta = 30^\circ$ and (c) $\beta = 53^\circ$. (d) The representative longitudinal slip and (e) transverse slip systems. Note that slip direction is denoted by $s^{(\alpha)}$ and slip plane normal $m^{(\alpha)}$.

non-zero fibre rotation angle, equal to half of the engineering shear strain, $\gamma/2$, would be predicted. In the classical Hill's yielding criteria, the elastic and plastic strain is decomposed additively with an associated flow rule. The two key assumptions of Hill's plasticity model are: (i) the material symmetries remain unchanged upon plastic deformation (ii) the kinematics of fibres are identical to the lamina. Hence the rotation of the local fibre coordinate system with respect to the global coordinate system is equal to the spin (rotation) component of the total deformation gradient. Under these assumptions, the plastic shear strain is symmetric hence there is no difference between γ_{12}^p and γ_{21}^p . The plastic spin (rotation) is always zero with the total spin (rotation) equals to the elastic spin (rotation). Therefore, regardless of the direction of the simple shear, a constant $\gamma_{12}/2$ will be predicted.

However, a significant fibre rotation towards the loading direction is observed when shear loading is applied perpendicular to the fibre orientation. This effect is becoming more evident when shear loading is applied to a cross-ply composite laminates [1,8]. The reorientation of fibres results in large plastic deformation of the composites. Therefore, our model needs to capture both matrix shearing deformation along fibre direction and fibre rotation.

2.2. Model assumptions

Experimental observations suggest that slip deformations are mainly in the matrix-rich regions or fibre-matrix interfaces [1,8,41,42]. By analogy, we adopt the classical framework of crystal plasticity [43,44], where the plastic deformation of a UD CFRP lamina is assumed to be due to fibre slip along certain slip systems within the matrix. To define the so-called 'crystal model' in this study, we use a similar notation as the crystal plasticity model. For each slip system α , we denote the slip direction vector $s^{(\alpha)}$ and the slip plane normal vector $m^{(\alpha)}$. For the local coordinate system (x_1, x_2, x_3) , x_1 aligns along the fibre direction and the (x_2, x_3) plane is perpendicular to the fibre direction. The choice of specific slip systems requires careful judgement. We therefore further classify the slip systems into longitudinal and transverse slip modes with each mode containing several slip systems (as shown in Fig. 1). The existence of longitudinal and transverse slip modes has been proved [1, 42]. Note that slip along system α_L represents the longitudinal slip of the lamina along the x_1 fibre direction, whilst α_T represents the transverse slip of the lamina within the (x_2, x_3) plane. To further investigate the effect of slip systems, we define β as the minimum angle between the x_3 axis and the slip direction of transverse slip system α_T .

Assuming the slip will only occur at the matrix-resin regions or fibre-matrix interfaces, several possible slip modes can be summarized from literature, based on the fibre-packing mode and microstructure of CFRP composites. The hexagonal closed packed (HCP) structure [45] within the (x_2, x_3) plane would result in α_T with $\beta = \pm 30^\circ$. When carbon fibres are not hexagonal closed packed, other potential slip directions may exist depending on the yield criteria. Tresca's yield criterion [46] predicts transverse slip directions with angles $\beta = \pm 45^\circ$, where the material reaches its maximum shear stress. Puck's failure criterion [47] resembling the Mohr–Coulomb fracture hypothesis [48] suggests the transverse slip direction is around $\beta = \pm 53^\circ$. Puck's model introduces an additional fracture-resistance term assuming the occurrence of internal friction. At the micro-mechanical level, the internal friction results from the normal stress acting on the micro-cracks in the matrix before the initiation of macroscopic cracks [47]. Experimental results [41] as well as computational predictions [42,47,49,50] on the transverse compression failure of UD CFRP lamina also prove that the matrix is prone to fail along a certain plane of angle β in the range of $53^\circ \pm 3^\circ$. Based on these physical considerations, we proceed to investigate the effect of transverse slip systems by selecting three groups of slip systems as follows:

- (1) $\beta = 45^\circ$: Two longitudinal and four transverse slip systems (Tresca).
- (2) $\beta = 30^\circ$: One longitudinal and three transverse slip systems (HCP).
- (3) $\beta = 53^\circ$: One longitudinal and two transverse slip systems (Puck)

We have defined three groups of representative slip systems, as shown in Fig. 1. The full slip systems for each group are shown in Fig. 1a, b and c respectively. The vectors of slip direction and slip plane normal for each group of slip systems are given in Table 1, Table 2 and Table 3 respectively. The notation of the slip systems is explained by the typical longitudinal and transverse slip systems, illustrated in Fig. 1d and e. For longitudinal slip system $\alpha = (1)$, the slip direction $(1, 0, 0)$ is aligned with the x_1 axis, while the slip plane normal $(0, 0, 1)$ is along with the x_3 axis. Likewise, in the transverse slip system $\alpha = (5)$, the slip direction $(0, \cos \beta, \sin \beta)$ is in line with an inclined angle of β with respect to the x_3 axis, while the slip plane normal $(0, -\sin \beta, \cos \beta)$ is the normal vector of the plane that is perpendicular to the slip direction. Therefore, the dot product of slip direction vector $s^{(\alpha)}$ and slip plane normal vector $m^{(\alpha)}$ is zero.

The effect of slip orientations on the mechanical response of UD CFRP subjected to uniaxial transverse compression is discussed later in Section 4.2. It is emphasised that the precise orientation of slip systems depends on an accurate characterisation of composite microstructures (fibre distribution, fibre volume fraction, void contents, fibre/matrix interfacial properties [51] etc.) which of course is dependent on statistical variation.

2.3. Kinematics

Consider a UD CFRP lamina as shown in Fig. 2 with fibre direction aligned along the x_1 coordinate. The total deformation gradient F_{ij} which maps the original configuration Ω_0 to the deformed configuration Ω is multiplicatively decomposed into a plastic part F_{ij}^p which maps Ω_0 to an intermediate, stress free configuration Ω_i , and an elastic part F_{ij}^e which maps Ω_i to Ω . Such that

$$F_{ij} = F_{ik}^e F_{kj}^p. \quad (1)$$

The plastic deformation of the lamina F_{ij}^p is characterised by the internal state variable γ^α representing the fibre slip along each individual slip system α . Let $s_i^{(\alpha)}$ and $m_k^{(\alpha)}$ denote the slip direction and slip plane normal vector respectively, F_{ij}^p is then defined in the rate form,

$$\dot{F}_{ij}^p = \sum_{\alpha=1}^N \dot{\gamma}^{(\alpha)} s_i^{(\alpha)} m_k^{(\alpha)} F_{kj}^p. \quad (2)$$

The rate form of plastic deformation gradient can be related by the plastic component of the deformation gradient and the corresponding velocity gradient L_{ij}^p via $\dot{F}_{ij}^p = L_{ik}^p F_{kj}^p$. The velocity gradient L_{ij}^p associated with plastic shearing on the slip systems is given by,

Table 1
Slip direction vectors and slip plane vectors for slip system group $\beta = 45^\circ$.

Slip systems α		Slip direction $s^{(\alpha)}$	Slip plane normal $m^{(\alpha)}$
Longitudinal slip systems	(1)	(1, 0, 0)	(0, 0, 1)
	(2)	(1, 0, 0)	(0, 1, 0)
	(3)	(0, 1, 0)	(0, 0, -1)
	(4)	(0, 0, 1)	(0, 1, 0)
	(5)	$(0, \frac{\sqrt{2}}{2}, \frac{\sqrt{2}}{2})$	$(0, \frac{\sqrt{2}}{2}, -\frac{\sqrt{2}}{2})$
Transverse slip systems	(6)	$(0, -\frac{\sqrt{2}}{2}, \frac{\sqrt{2}}{2})$	$(0, \frac{\sqrt{2}}{2}, \frac{\sqrt{2}}{2})$
		$(\frac{\sqrt{2}}{2}, \frac{\sqrt{2}}{2}, 0)$	

Table 2
Slip direction vectors and slip plane vectors for slip system group $\beta = 30^\circ$.

Slip systems α		Slip direction $s^{(\alpha)}$	Slip plane normal $m^{(\alpha)}$
Longitudinal slip systems	(1)	(1, 0, 0)	(0, 0, 1)
Transverse slip systems	(2)	(0, 1, 0)	(0, 0, -1)
	(3)	$(0, \frac{1}{2}, \frac{\sqrt{3}}{2})$	$(0, \frac{\sqrt{3}}{2}, -\frac{1}{2})$
	(4)	$(0, -\frac{\sqrt{2}}{2}, \frac{\sqrt{2}}{2})$	$(0, \frac{\sqrt{2}}{2}, \frac{\sqrt{2}}{2})$

Table 3
Slip direction vectors and slip plane vectors for slip system group $\beta = 53^\circ$.

Slip systems α		Slip direction $s^{(\alpha)}$	Slip plane normal $m^{(\alpha)}$
Longitudinal slip systems	(1)	(1, 0, 0)	(0, 0, 1)
Transverse slip systems	(2)	(0, 1, 0)	(0, 0, -1)
	(3)	(0, 0.8, 0.6)	(0, 0.6, -0.8)

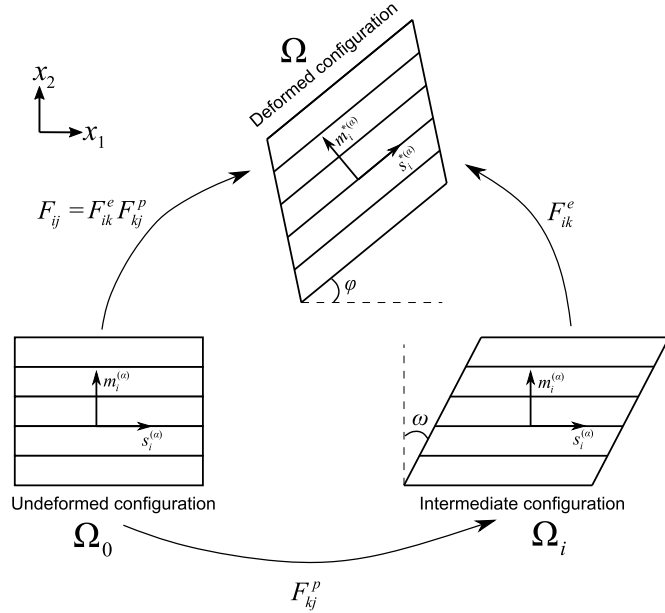


Fig. 2. Multiplicative decomposition of the total deformation gradient into elastic and plastic component.

$$L_{ij}^p = \sum_{\alpha} \dot{\gamma}^{(\alpha)} s_i^{(\alpha)} m_j^{(\alpha)}. \quad (3)$$

The updated plastic deformation gradient at a certain time increment Δt is calculated as,

$$F_{ij}^{p, t+\Delta t} = F_{ij}^p \Delta t + F_{ij}^{p, t}. \quad (4)$$

The vectors $s_i^{(\alpha)}$ and $m_i^{(\alpha)}$ are assumed to convect with the lamina so in the deformed configuration Ω they become $s_i^{(\alpha)*}$ and $m_i^{(\alpha)*}$,

$$s_i^{(\alpha)*} = F_{ij}^e s_j^{(\alpha)}, \quad (5)$$

$$m_i^{(\alpha)*} = m_j^{(\alpha)} (F_{ji}^e)^{-1}. \quad (6)$$

One of the goals of this paper is to understand the effect of fibre rotation on the stress-strain response, hence here we propose a way to

evaluate the fibre rotation φ from the kinematic relation. Recall the plastic deformation, and consequently, plastic spin does not change the fibre direction, therefore, φ can be evaluated from the elastic rotation R_{ij}^e of the lamina which is given by,

$$R_{ij}^e = F_{ik}^e (U_{jk}^e)^{-1}, \quad (7)$$

where R_{ij}^e is the rotation matrix, and U_{jk}^e is the right stretch tensor.

The fibre rotation φ is then calculated as,

$$\varphi = \tan^{-1} (R_{ij}^e, R_{ii}^e) \quad (8)$$

The elastic Green strain E_{ij}^e is given by:

$$E_{ij}^e = \frac{1}{2} (F_{ki}^e F_{kj}^e - \delta_{ij}), \quad (9)$$

where δ_{ij} is the Kronecker delta.

2.4. Constitutive law

The UD lamina is assumed to be elastic and transversely isotropic. We define a material stress measure Σ_{ij} in the intermediate configuration such that it is work conjugate to the elastic Green strain E_{ij}^e . A linear elastic relationship is assumed between Σ_{ij} and E_{ij}^e with the elastic constitutive relationship written as,

$$\begin{pmatrix} E_{11}^e \\ E_{22}^e \\ E_{33}^e \\ E_{23}^e \\ E_{13}^e \\ E_{12}^e \end{pmatrix} = \begin{pmatrix} \frac{1}{E_f} & -\nu_{21} & -\nu_{31} & 0 & 0 & 0 \\ \frac{-\nu_{12}}{E_f} & \frac{1}{E_{m2}} & \frac{-\nu_{32}}{E_{m3}} & 0 & 0 & 0 \\ \frac{-\nu_{13}}{E_f} & \frac{-\nu_{23}}{E_{m2}} & \frac{1}{E_{m3}} & 0 & 0 & 0 \\ 0 & 0 & 0 & \frac{1}{2G_{23}} & 0 & 0 \\ 0 & 0 & 0 & 0 & \frac{1}{2G_{13}} & 0 \\ 0 & 0 & 0 & 0 & 0 & \frac{1}{2G_{12}} \end{pmatrix} \begin{pmatrix} \Sigma_{11} \\ \Sigma_{22} \\ \Sigma_{33} \\ \Sigma_{23} \\ \Sigma_{13} \\ \Sigma_{12} \end{pmatrix}, \quad (10)$$

where E_f is the longitudinal modulus of a UD lamina, E_{m2} and E_{m3} are the transverse moduli of the UD lamina in the x_2 and x_3 direction respectively. G_{ij} and ν_{ij} are the shear moduli and Poisson ratios respectively. Note that $G_{23} = 0.5E_{m2}/(1+\nu_{23})$ as a transversely isotropic material. The relationship between Cauchy stress σ_{ij} and material stress Σ_{ij} is given by:

$$\Sigma_{ij} = \det(F_{ij}^e) (F_{ik}^e)^{-1} \sigma_{kl} (F_{jl}^e)^{-1}. \quad (11)$$

It now remains to define the plastic constitutive relationship. Following Asaro and Needleman [43], the evolution of the shear strain $\gamma^{(\alpha)}$ is given by a rate-dependent power law relationship,

$$\dot{\gamma}^{(\alpha)} = \dot{\gamma}_0 \left(\frac{\tau^{(\alpha)}}{\tau_y^{(\alpha)}} \right)^n \text{sgn}[\tau^{(\alpha)}], \quad (12)$$

where $\tau^{(\alpha)}$ denotes the thermodynamic driving force for the shear strain rate $\dot{\gamma}^{(\alpha)}$, while τ_y and $\dot{\gamma}_0$ denotes the shear yield strength and the reference shear strain rate of the lamina respectively. n is a rate sensitivity exponent and $\text{sgn}[\cdot]$ returns the sign of resolved shear stress. In classical crystal plasticity [44], the resolved shear stress $\tau^{(\alpha)}$ is evaluated from the Schmid's law,

$$\tau^{(\alpha)} = s_i^{(\alpha)*} \sigma_{ij} m_j^{(\alpha)*}. \quad (13)$$

However, literature has shown that the yield strength of matrix

material is pressure sensitive [52,53]. The pressure dependency is characterised by the friction coefficient μ and the in-plane normal pressure P introduced on the slip systems, as adopted by Meza et al. [32] to model the pressure-dependent shear behaviour of 3D non-woven carbon fibre reinforced composites. This is similar to Mohr-Coulomb theory, such that the shear strength of a slip system α is given by,

$$\tau_y^{(\alpha)} = \begin{cases} \tau_y + \mu P & P \geq 0 \\ \tau_y & P < 0 \end{cases} \quad (14)$$

where τ_y is the shear yield strength absent pressure effect.

As we assume the lamina is elastic along the fibre (x_1) direction, the pressure P is defined in the x_2 - x_3 plane and is given by:

$$P = -\frac{1}{2}(\Sigma_{22} + \Sigma_{33}). \quad (15)$$

2.5. Strain rate effect

Experiments [4,5,39] have shown that the transverse modulus E_{m2} (in x_2 direction) and E_{m3} (in x_3 direction), the shear modulus G_{ij} ($i, j = 1, 2, 3, i \neq j$) as well as the shear yield strength τ_y of CFRP composites is strain rate sensitive. Here the scaling functions [4,39] to capture the strain rate dependency of the modulus and strength are given by,

$$E_{m2} = E_{m2}(\dot{\epsilon}_0) \left(m \text{Log}_{10} \frac{\dot{\epsilon}_{22}}{\dot{\epsilon}_0} + 1 \right) \quad (16)$$

$$E_{m3} = E_{m3}(\dot{\epsilon}_0) \left(m \text{Log}_{10} \frac{\dot{\epsilon}_{33}}{\dot{\epsilon}_0} + 1 \right) \quad (17)$$

$$G_{ij} = G_{ij}(\dot{\gamma}_0) \left(m \text{Log}_{10} \frac{\dot{\gamma}_{ij}}{\dot{\gamma}_0} + 1 \right) \quad (18)$$

where $\dot{\epsilon}_0$ is the quasi-static strain rate of $1 \times 10^{-4}/s$, $\dot{\gamma}_0$ is the quasi-static shear strain rate of $2 \times 10^{-4}/s$, $\dot{\epsilon}_{ij}$ ($i, j = 1, 2, 3, i \neq j$) are the rate form of total green strain tensors. The material rate sensitivity m is found to be the same for the transverse and shear modulus from the dynamic measurements [39].

The strain rate dependency of shear yield strength is incorporated in the model via the power law relationship specified in Eq. (12). It relates the shear strain rate to the shear yield strength of UD lamina. The strain rate dependency for shear yield strength n is calibrated against the measured data [4,39] via a rearranged form of Eq. (12), as given by,

$$\tau_y(\dot{\gamma}) = \tau_y(\dot{\gamma}_0) \frac{1}{n} \text{Log}_{10} \frac{\dot{\gamma}_{ij}}{\dot{\gamma}_0}, \quad (19)$$

where $\tau_y(\dot{\gamma}_0)$ and $\tau_y(\dot{\gamma})$ are the shear yield strengths at the quasi-static strain rate and a given strain rate respectively, $\dot{\gamma}_{ij} = \dot{\epsilon}_{ij}$ is the total shear strain rate of the material. Note that we only need to define the rate-dependency of shear yield strength, since compressive failure of UD lamina is also governed by shear-dominated failure, as discussed in Section 4.2. This phenomenon is also verified by dynamic measurements [39], where the ratio of the transverse compressive strength σ_y to the shear yield strength τ_y is found to be approximately constant and independent of strain rate.

3. Model implementation

3.1. Numerical implementation

The material model is implemented in ABAQUS Explicit (version 6.14) via the user subroutine VUMAT. The full algorithm is detailed in Appendix A. In brief, the subroutine collects the deformation gradient tensors and right stretch tensors, followed by the initialisation of slip systems for each integration point. Then intermediate stresses, Cauchy

stresses, local shear strain rates and deformation gradient components are calculated for each slip system in a clockwise loop according to Fig. 3. During the calculation process, the analysis calculates the resolved shear stresses of each slip system. Once any shear stress in the slip system reaches its critical resolved shear stress, the slip is activated and plastic flow is initiated. As the load increases, the resolved shear stress on each system increases until the pressure-dependent shear yield strength $\tau_y^{(\alpha)}$ is reached on one system. The fibre composite begins to plastically deform by slip on this system, so-called 'primary slip system'. As the load is increased further, $\tau_y^{(\alpha)}$ may be reached on other slip systems; these systems then begin to operate. Multiple slips may occur simultaneously during the loading process. Once the calculation loop finishes in each time increment, the subroutine will update the local plastic shear strain rates, deformation gradients and slip systems. The fibre rotation angle will be stored as a state variable. The whole process is repeated for each element at every time increment.

3.2. Materials properties

The UD lamina of IM7-8552 carbon fibre composites is modelled as an anisotropic, homogenised continuum with its microstructure and slip systems defined. The shear yielding of a lamina that is controlled by matrix is defined by isotropic elastic, perfectly-plastic behaviour that satisfies the Von Mises yield criterion (J_2 flow theory). The longitudinal modulus E_f , transverse modulus E_m (E_{m2} or E_{m3}), shear modulus G_{ij} ($i, j = 1, 2, 3, i \neq j$), and shear yield strength τ_y of the lamina are measured from experiments. A summary of strain rate-dependent moduli C_{ij} (E_{m2} , E_{m3} or G_{ij}) and shear yield strength τ_y as measured from experiment [4, 39,40] is plotted in Fig. 4, where rate-dependent parameters m and n are obtained from the curve fitting of modulus data. Material constants used for the finite element simulation are given in Table 4. The friction coefficient μ is chosen to be 0.28 according to Ref. [1].

3.3. Finite element simulation

All the finite element simulations have been carried out in parallel using 4 CPUs (Inter-Core-i7-6700, 3.4 GHz). 3D solid elements with reduced integration (C3D8R in ABAQUS notation) are used in the constitutive model, while continuum shell elements are used in the Hashin damage model [54] to compare their computation costs. Surface contact has been defined between the adjacent plies in the cross-ply laminates (CP), while no surface contact is defined for the unidirectional laminates (UD). Off-axis compression (comp) on UD laminates, uniaxial tension and compression applied to CP laminates were conducted in this study. Mass scaling that reduces the simulation time is especially useful for the rate-dependent material [55]. No mass scaling is

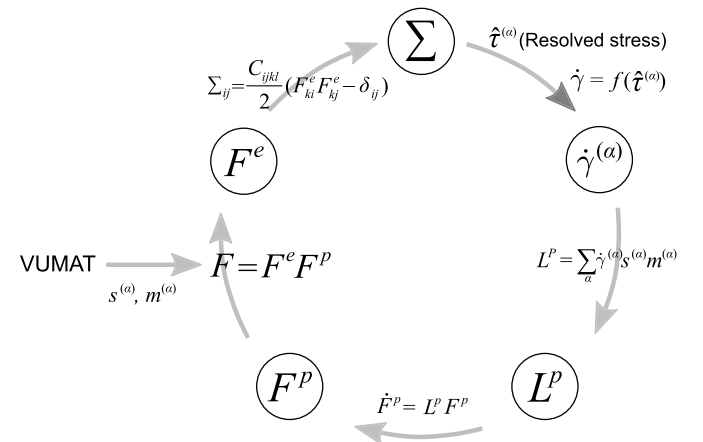


Fig. 3. Flow chart for the model implementation.

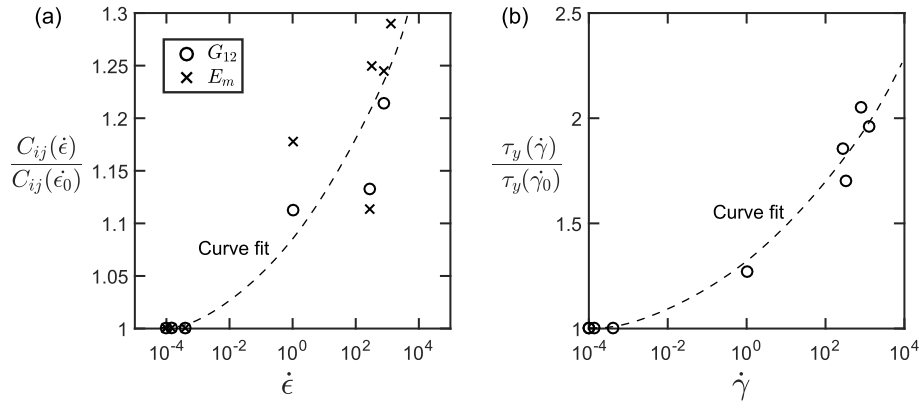


Fig. 4. (a) Normalised transverse and shear modulus (b) Normalised shear yield strength as a function of strain rate. Data are taken from Ref. [4,5,39,40].

Table 4

Material parameters for finite element simulation of IM7-8552 carbon fibre composites [4,39,40].

Material properties	Quasi-static ($\dot{\epsilon}=0.0004 \text{ s}^{-1}$)
E_f	171.42 GPa
ν_{21}	0.01667
ν_{12}	0.32
ν_{23}	0.34
E_{m2}	8.93 GPa
E_{m3}	8.93 GPa
G_{12}	5.10 GPa
μ	0.28
τ_y	62.3 MPa [4], 85 MPa [5]
σ_{my}	104 MPa
m	0.035
n	22.4

used in the high strain rate (HS) rate simulation, whilst mass scaling is used in the quasi-static (QS) rate simulation such that the scaled-up loading rate associated with mass scaling is 100 mm/s, at about 10^{-5} of the wave speed of the carbon fibre composites (10 km/s). The loading velocities for UD and CP laminates in the experiments are 8×10^{-3} mm/s and 4×10^{-3} mm/s respectively. Therefore, the mass scaling factor for the UD-QS-Comp is 1.56×10^8 , while for the CP-QS-Comp and CP-QS-Tension is 6.25×10^8 . The literature suggests that the scaled-up loading rate should not exceed 1% of the wave speed [55], which is 1000 times larger than the scaled loading rates in our simulation. Therefore, the effect of mass scaling we used is almost negligible and has been confirmed by comparing with the stress-strain curve results obtained from smaller mass scaling factors.

4. Finite element prediction

This section presents the predictive capabilities of the crystal plasticity model regarding the non-linear response of composite laminates. The geometrical hardening effect is explained by an analytical model of simple shear test with a single element in Section 4.1. The effect of slip orientation on the transverse compressive response of a single element is shown in Section 4.2. Numerical results of off-axis compression tests of UD lamina under various strain rates is then compared against the experimental results in Section 4.3. Finally, the capability of this physically-based model, to capture the non-linear response of CP composite laminates, is demonstrated in Section 4.4.

4.1. Simple shear tests of UD lamina

Simple shear loading parallel and perpendicular to the fibre orientation, see Fig. 5a, were applied to a UD lamina (single element) under quasi-static deformation ($\dot{\gamma} = 10^{-4}/\text{s}$). The corresponding stress-strain curves are plotted in Fig. 5b. Recall that the epoxy matrix is assumed to be elastic perfectly plastic. For simple shear parallel to fibre direction, these curves predicted by the ‘crystal model’ capture the perfectly-plastic behaviour accurately. The prediction from Hill’s anisotropic yield criterion [23] under quasi-static rate is also shown in Fig. 5b. Hill’s model predicts an identical response for shear parallel and perpendicular to the fibre directions under quasi-static loading. It captures the initial yielding behaviour and matches the results predicted by the crystal plasticity model under small strain deformation. However, for shear strain $\gamma > 8\%$, the stress-strain curve shows a downward trend, which is not physical compared to measurement. The two key assumptions of Hill’s plasticity model that lead to poor predictions of UD composite under simple shear loading are: (i) the material symmetries remain unchanged upon plastic deformation (ii) the kinematics of fibres are identical to the lamina. Hence the rotation of the local fibre coordinate system with respect to the global coordinate system is equal to the spin component of the total deformation gradient. In this simple shear case, Hill’s model will rotate the local coordinates by $\gamma_{xy}/2$ even though the fibre rotation is zero, hence leading to errors in the prediction of the finite deformation of composite lamina.

For simple shear perpendicular to the fibre orientation, significant hardening behaviour is observed, which is consistent with shear experiments on UD lamina [1] and computational micromechanics prediction [42]. Assuming a perfect-bond between fibre and matrix, we derive the shear stress τ_{xy} as a function of total shear strain γ_{xy} below based on crystal plasticity framework (see the detailed derivation in Appendix B),

$$\tau_{xy} = \begin{cases} G_{12}\gamma_{xy} & \gamma_{xy}^p = 0 \\ \tau_y + 0.5E_f\gamma_{xy}^3 & \gamma_{xy}^p > 0 \end{cases}, \quad (20)$$

where $\gamma_{xy} = \tan \omega$ is the total shear strain, γ_{xy}^p the plastic strain and E_f the longitudinal modulus of composite lamina. The hardening behaviour is controlled by the term $0.5E_f\gamma_{xy}^3$, which is the product of the longitudinal modulus of composite lamina E_f (dominated by the fibre modulus) and the cube of shear strain γ_{xy} (indicating fibre rotation φ). The finite element prediction and analytical prediction achieves a good correlation in Fig. 5b, confirming the accuracy of our crystal-plasticity based model. Physically, since matrix deformation could not progress independently of the fibres, significant fibre rotation is generated to accommodate the shear strain in the matrix and inherently increases the Cauchy stress and corresponding resolved shear stress, see Eq. (20). Consequently, a

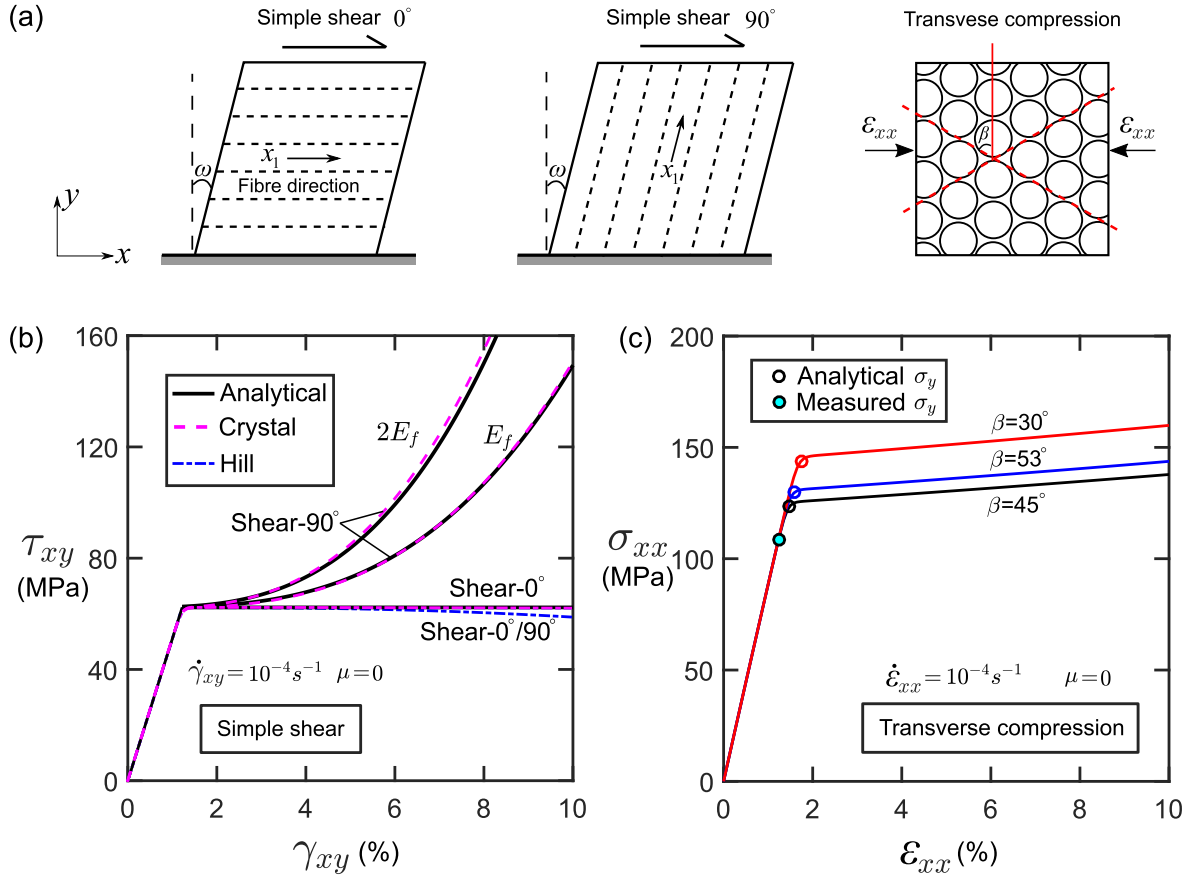


Fig. 5. (a) Sketches of boundary conditions: simple shear 0°, simple shear 90°, transverse compressive tests of a unidirectional lamina. (b) Predicted stress-strain curves of simple shear on a unidirectional lamina using the crystal plasticity model and Hill's model. (c) Predicted stress-strain curves of a unidirectional lamina under transverse compression of slip system oriented at $\beta = 45^\circ, 53^\circ, 30^\circ$ respectively.

significant geometrical hardening response of the composite lamina under finite deformation is observed. We have also shown the hardening effect is enhanced through increasing the longitudinal modulus from E_f to $2E_f$ in Fig. 5b. However, due to possible fibre-matrix debonding or matrix cracking, the measured stress-strain curves of shearing perpendicular to fibre direction [1] only shows a limited strain hardening behaviour. A significant strain hardening behaviour is evident in the cross-ply composite laminates due to the constraining effect of the adjacent plies. The predicted difference in simple shearing parallel and transverse to fibres is supported by the physically-based FE analysis [8] and experimental measurements [56].

4.2. Transverse compression tests of UD lamina

The Mohr–Coulomb model suggests the deformation of a composite lamina under transverse compression forms fracture plane of an angle β with a plane perpendicular to the loading axis [41], see Fig. A1. Similarly, in our crystal plasticity model, we define slip directions β . Applying a uniaxial transverse compression to a composite lamina, the transverse compressive yield strength of the composite lamina σ_y is related to the critical resolved shear stress $\tau_y^{(a)}$, see Appendix C, as follows,

$$\sigma_y = \frac{2\tau_y^{(a)}}{\sin 2\beta} \quad (21)$$

To investigate the effect of slip orientation β upon the uniaxial compressive response of the composite lamina, virtual uniaxial compressive tests were conducted on a composite lamina with various slip systems, $\beta = 30^\circ, 45^\circ$ and 53° . Their stress-strain responses are

shown in Fig. 5c. Note that for the case of friction coefficient $\mu = 0$, $\tau_y^{(a)}$ equals the shear strength of the matrix $\tau_y = 62.3$ MPa. The compressive yield strength increases with the slip orientation changing from 45° to 30° . The predicted yield strength with slip triggered at 45° is the closest prediction to the measured yield strength $\sigma_{my} = 104$ MPa [4]. In order to obtain accurate slip plane angles, Brent's algorithm that combines a golden section search with parabolic interpolation can be used in the future [12], including the constraint that fracture planes mainly initiate and propagate along the fibre-matrix interface. For simplicity, the slip orientation in the transverse $x_2 - x_3$ plane is set to be 45° for the following simulations. Fig. 5c shows that compressive yield strengths predicted by FE are in a good agreement with the analytical solutions from Eq. (21), which confirms that the matrix shearing governs the transverse compression behaviour of a UD composite lamina.

4.3. Off-axis compression tests of UD composite lamina

In order to verify our model, we compare the finite element predictions with the measured stress-strain responses of a unidirectional (UD) composite lamina subjected to quasi-static and dynamic off-axis compressive loading, as shown in Fig. 6a.

4.3.1. Mesh-dependency study

The dependency of mesh size used in the finite element calculation is demonstrated for off-axis compressive tests of UD composite laminates with fibres orientated at $\theta = 15^\circ$ and 45° . These geometries were meshed using eight-node brick elements (C3D8R in the ABAQUS notation). Shear strain contours γ_{12} are plotted in Fig. 7a and Fig. 7b. A uniform shear band is evident in each loading case with the bandwidth

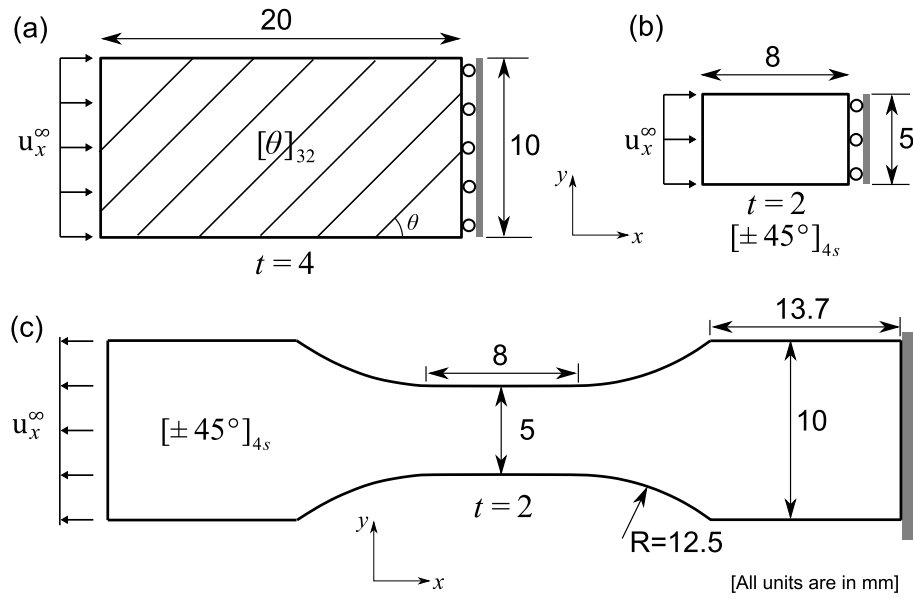


Fig. 6. Specimen geometries, for (a) IM7-8552 unidirectional composite laminates of different off-axis angle subjected to uniaxial compressive loading [4], $[\pm 45^\circ]_{4s}$ composite laminates under (b) uniaxial compressive and (c) tensile loading [5], all units are in mm. Note that thickness is denoted by t .

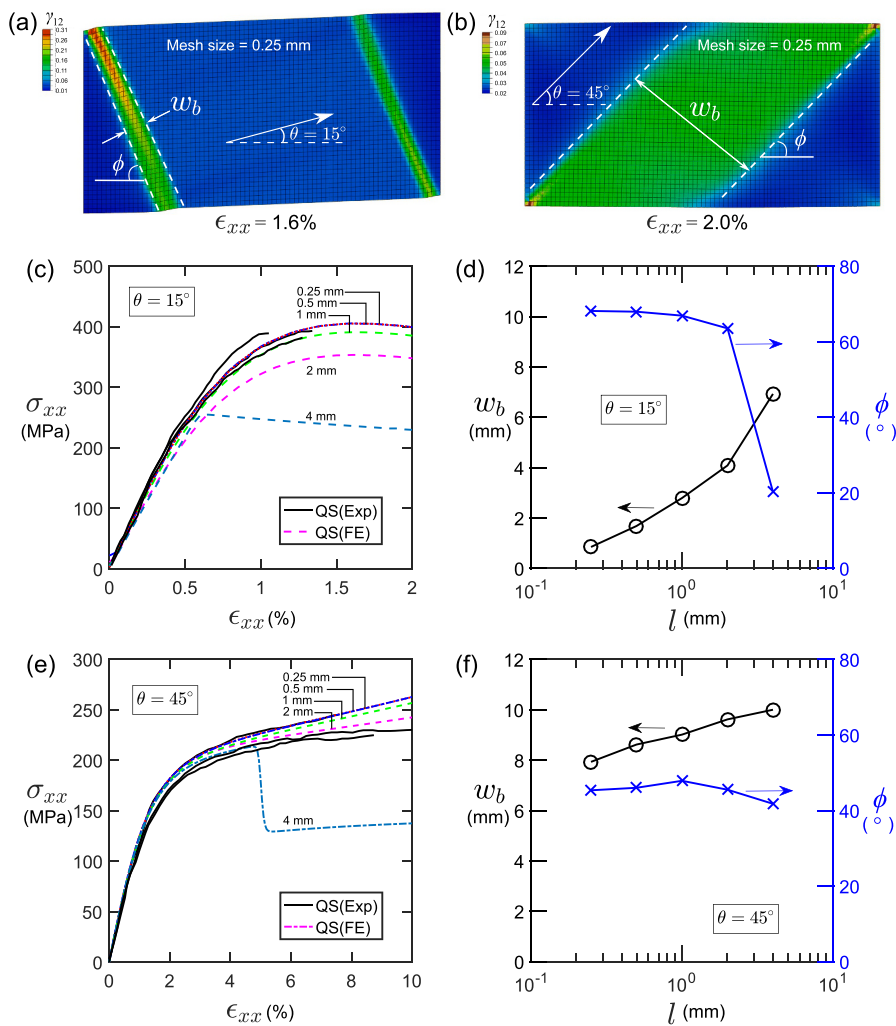


Fig. 7. Mesh-dependency study of the finite element model under quasi-static (QS) loading: shear strain contours of specimens under off-axis compressive loading at (a) $\theta = 15^\circ$ and (b) $\theta = 45^\circ$ using 0.25 mm mesh; stress-strain responses of off-axis compressive loading at (c) $\theta = 15^\circ$ and (d) $\theta = 45^\circ$ using meshes from 0.25 mm to 4 mm; shear bandwidth w_b and the kink angle ϕ between the shear band with respect to loading axis are plotted against mesh size of off-axis angle (d) $\theta = 15^\circ$ and (f) $\theta = 45^\circ$ respectively.

denoted as w_b . The shear band angle is defined between the shear band and the loading direction, denoted as ϕ . The stress-strain curves of these off-axis compressive tests using 3D cubic meshes of 0.25 mm, 0.5 mm, 1 mm, 2 mm and 4 mm are shown respectively in Fig. 7c and e. For a sufficiently small element size $l < 0.5$ mm, the stress-strain response is not significantly influenced by element size. The observed mesh dependency of the stress-strain is mainly governed by the inaccurate geometric description of coarse meshes. As the mesh is refined, the band angle reaches a converged value, see Fig. 7d and f. The maximum shear bandwidth predicted from FE decreases with the decreasing mesh size, which is dependent on the geometric length scale (e.g. fibre diameter) [57]. Similar mesh-independent results have been confirmed in the other off-axis loading directions and strain rates. For consistence, the mesh size is set to be 0.5 mm for the following FE simulations.

4.4. Strain rate effect

Virtual off-axis compressive tests on composite laminates with fibre orientation angles $\theta = 15^\circ, 30^\circ, 45^\circ, 60^\circ, 75^\circ$ and 90° (transverse compression) were conducted. Quasi-static (QS) loading $\dot{\epsilon}_{QS} = 4 \times 10^{-4}$ /s and high strain (HS) rate loading $\dot{\epsilon}_{HS}$ of 331/s were applied to these samples. All specimens have dimensions of $20 \times 10 \times 4$ mm³, see Fig. 6a.

The measured true stress-strain responses under off-axis compressive loading are compared with those predicted by our finite element model in Fig. 8. In broad terms, the predictions capture the modulus, yield strength and hardening behaviour in the experiment for all the off-axis tests under different strain rate loading. There are some scatter present in the experimental data for 15° off-axis compression tests, which show much stiffer responses than the numerical prediction.

Two localised shear bands were observed in the 15° off-axis

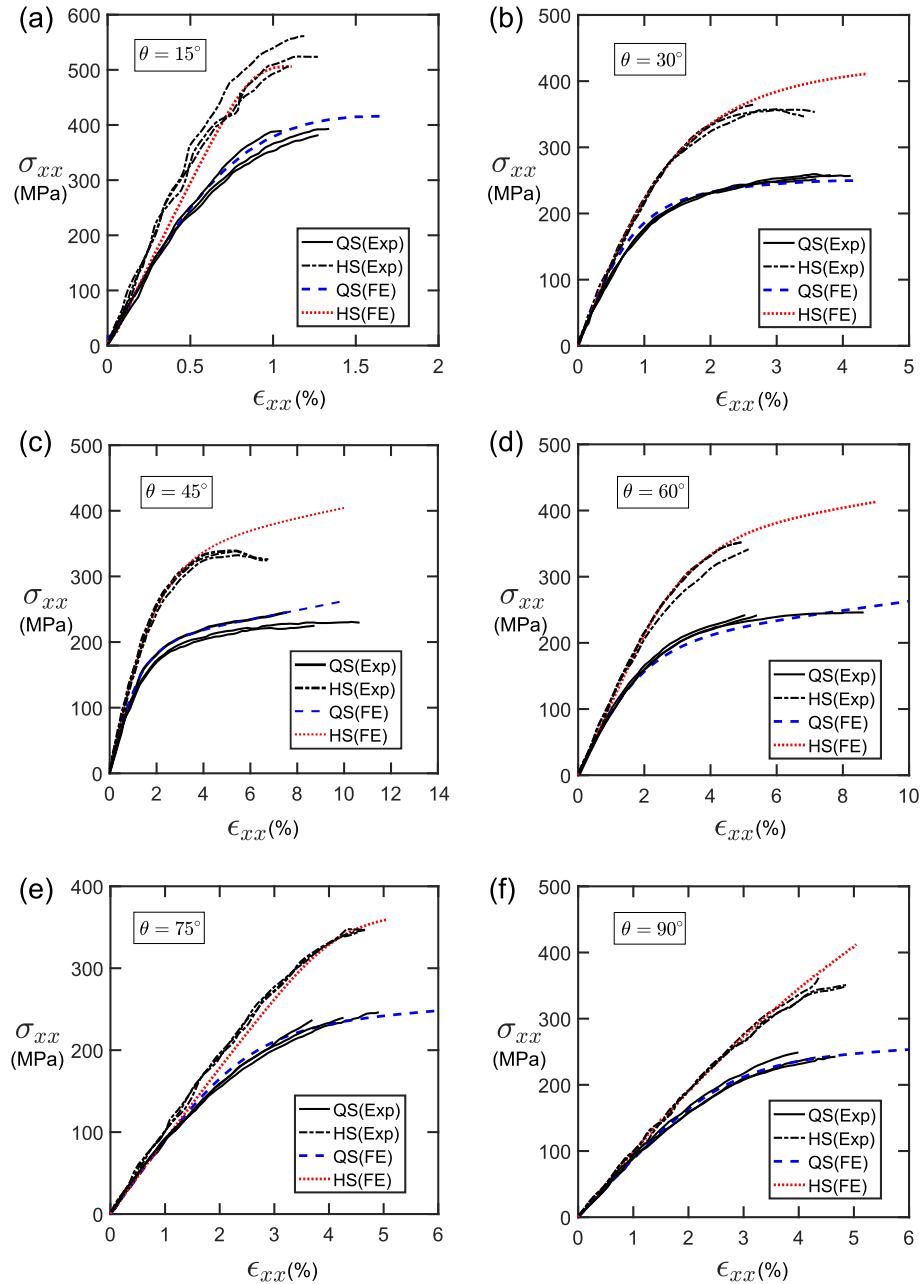


Fig. 8. Measured [4] and predicted uniaxial stress-strain responses for off-axis angle θ of (a) 15° (b) 30° (c) 45° (d) 60° (e) 75° (f) 90° compression tests under quasi-static (QS) and high strain rate (HS) loading.

compression tests. Composite fibres in the UD composite typically undergo kinking in a narrow band under axial compression. The origin of fibre kinking is plastic micro-buckling [57], which is initiated by the rotation and buckling of misaligned fibres. The predicted fibre rotation compared to measured values under quasi-static loading in Fig. 9a shows the accurate prediction of the fibre kinking effect. The numerical model enables the model to capture the plastic micro-buckling with a correct representation of plastic shear deformation and fibre rotation.

FE simulation accurately predicts a shear band developed in the 45° off-axis experimental tests, as shown in Fig. 9b. This is a failure mode essentially identical to the cracking in the bulk matrix material associated with the maximum shear stress, where fibres offer little resistance

to applied loading. For a transverse compression test in the 90° off-axis, typical $\pm 45^\circ$ shear bands indicating the transverse slips, were observed in the $x-z$ plane. The plastic shear strain shown in the FE prediction highlights the shear band similar with the experimentally observed fracture planes, see Fig. 9c.

Similar kinking failure for 15° sample, shear band for 45° sample and transverse failure for 90° sample are observed at both strain rates. Additionally, the stress-strain curves measured under quasi-static and dynamic loading are all showing the non-linear behaviour. However, there are some differences in terms of deformation mechanisms and failure behaviours. The strain distributions in the specimens are relatively uniform in the quasi-static loading cases whilst more localised

Uniaxial compression under quasi-static loading

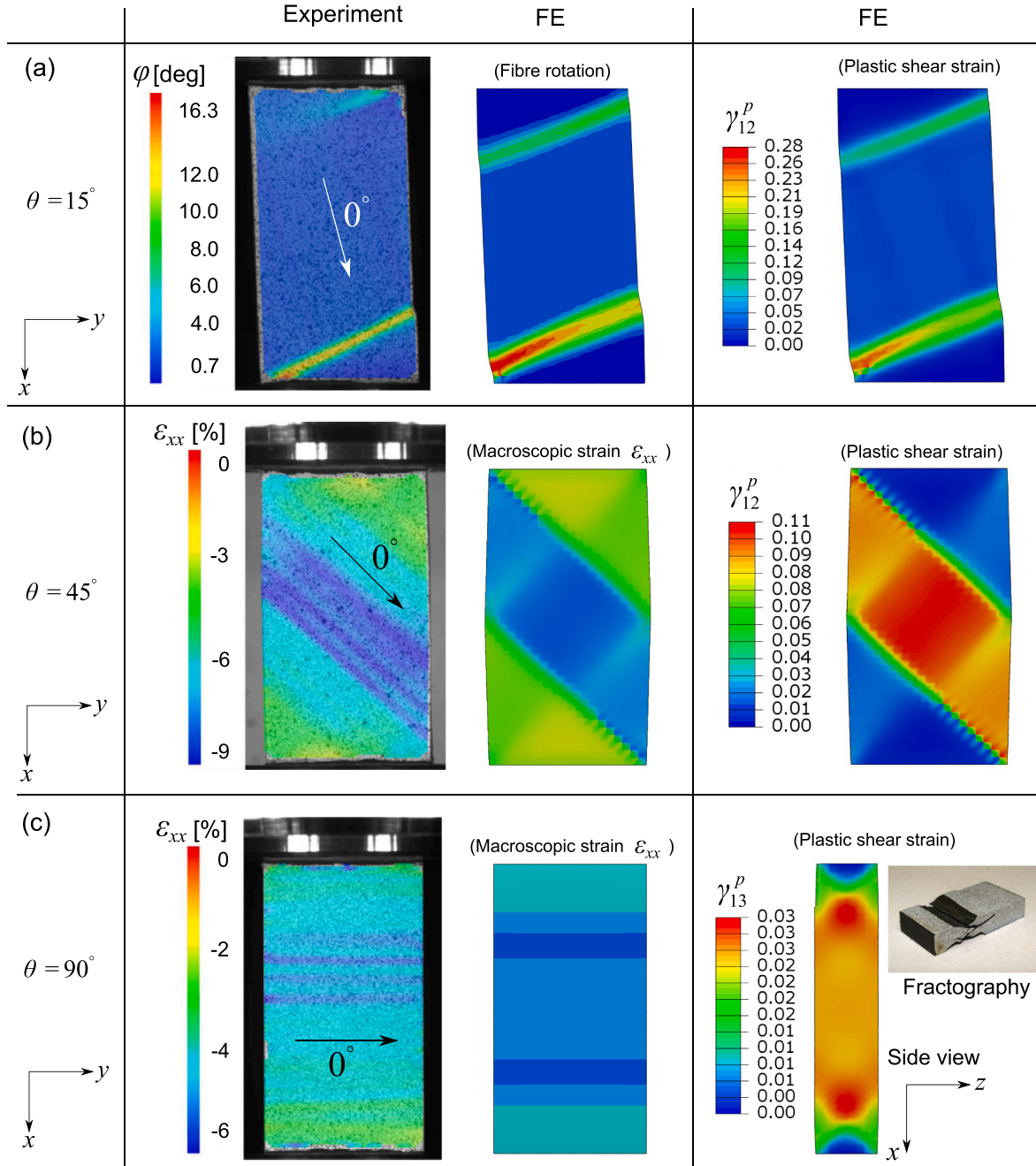


Fig. 9. Measured [4] and predicted fibre rotation, axial compressive strain and plastic shear strain contours for off-axis (a) $\theta = 15^\circ$ (b) $\theta = 45^\circ$ and (c) $\theta = 90^\circ$ compression tests subjected to quasi-static loading.

strain contours are observed in the dynamic loading cases. The shear band deformation spreads from one free edge to the other free edge, which may lead to some size-dependent behaviour for different strain rates. For the final fractography, specimens subjected to quasi-static loading in Fig. 9c suggests the fracture is relatively localised, while there are much more cracks in the samples subjected to dynamic loading as shown in Fig. 10c. This is probably due to the reduction in the fracture toughness of epoxy matrix at a higher strain rate [35]. The different failure mechanisms of composite materials under various strain rates are also observed in other relevant studies [58–61].

The predicted fibre rotations for 15° and 45° off-axis are shown in Fig. 10a and b. It should be noted that fibres rotate in anticlockwise direction. A localised band of fibre rotation was generated due to complementary shear stress perpendicular to fibre orientation, denoted by shear stress τ in Fig. 10b. Numerical results in 90° transverse compression predicts a shear band orientated at $\pm 45^\circ$, achieving a good qualitative correlation with experiment results in Fig. 10c.

4.4.1. Effect of frictional coefficient and hydrostatic pressure

The off-axis compression tests on 45° composite laminates is selected to investigate the effect of Mohr-Coulomb frictional coefficient μ and hydrostatic pressure p . Fig. 11a shows that friction coefficient only affects the level of yield stress, as expected from the constitutive model. The hydrostatic pressure dependency is switched off when the friction coefficient equals zero. Note that in all the other simulations, the hydrostatic pressure is set to be zero and $\mu = 0.28$.

To demonstrate the sensitivity of material response subjected to hydrostatic pressure, off-axis 45° compression tests under hydrostatic pressure from 0 MPa to 30 MPa were conducted. The hydrostatic

pressure is applied to all exterior surfaces of the specimen, as shown in Fig. 6b. The uniaxial compression is then applied by kinematic boundary conditions on the left and right surface of the specimen, whilst the lateral contraction of the specimen is not constrained. The predicted stress-strain curves in Fig. 11b reveal that both modulus and yield stress increases with the increasing hydrostatic pressure from 0 MPa to 30 MPa. This effect is similar to the pressure dependency observed for the composite materials Scotchply SP-319 [53].

4.5. Tensile and compressive tests of $[\pm 45^\circ]_{4s}$ composite laminates

4.5.1. Model validation

Now we proceed to validate our model via comparison with the measured stress-strain responses of $[\pm 45^\circ]_{4s}$ composite laminates, using the same matrix constants for IM7-8552 except that the shear strength is higher $\tau_y = 85$ MPa due to manufacturing variations (see Table 4). Virtual tensile and compressive tests on $[\pm 45^\circ]_{4s}$ laminates were conducted under quasi-static ($\dot{\epsilon}_{QS} = 5 \times 10^{-4}/s$) and dynamic loading ($\dot{\epsilon}_{HS} = 1300/s$) conditions. The dimension of the samples is specified in Fig. 6b and c. Perfect-bond between the neighbouring plies were defined for the laminates. Eight-node brick elements (C3D8R in the ABAQUS notation) with element size of 0.5 mm were used in the finite element models.

Fig. 12 shows the comparison between the experimental and numerical true shear stress-strain responses of $[\pm 45^\circ]_{4s}$ laminates under tensile and compressive loading. Significant fibre rotation was present in the experimental tensile tests of $[\pm 45^\circ]_{4s}$ laminates and contributed to the non-linear hardening behaviour. While the Hill's anisotropic yield model captures the initial yielding behaviour with a reasonable

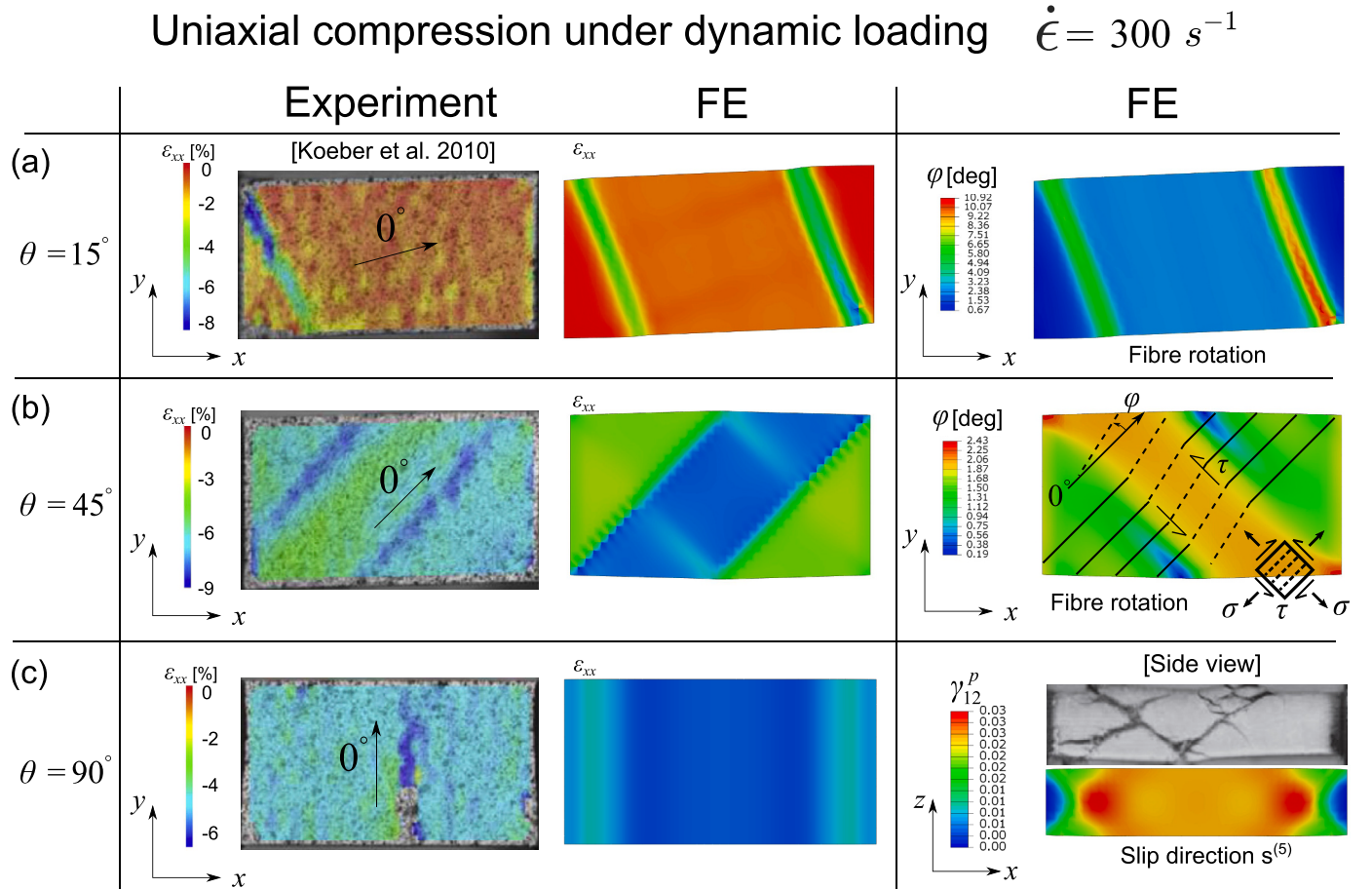


Fig. 10. Measured [4] and predicted axial compressive strain contours, fibre rotation and plastic shear strain for off-axis (a) $\theta = 15^\circ$ (b) $\theta = 45^\circ$ and (c) $\theta = 90^\circ$ compression tests subjected to dynamic loading. Note that anticlockwise direction is defined as positive for fibre rotation.

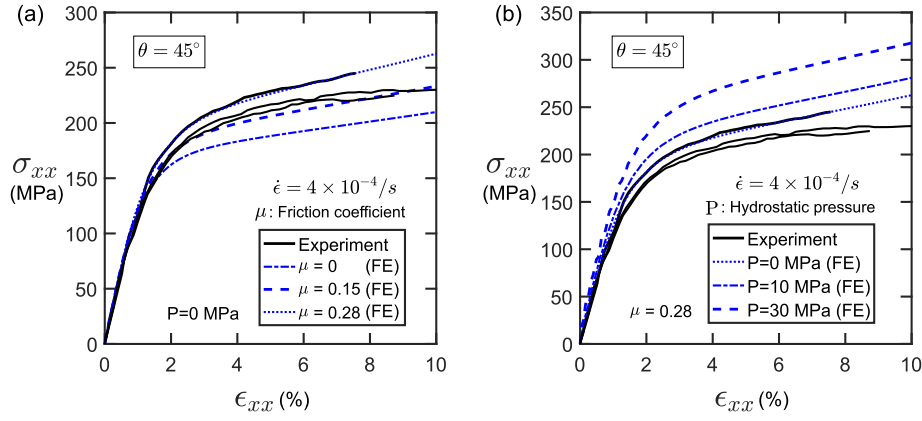


Fig. 11. The effect of (a) frictional coefficient and (b) hydrostatic pressure upon the stress-strain response of uniaxial compression tests on unidirectional laminates $[45^\circ]_{32}$ under quasi-static loading.

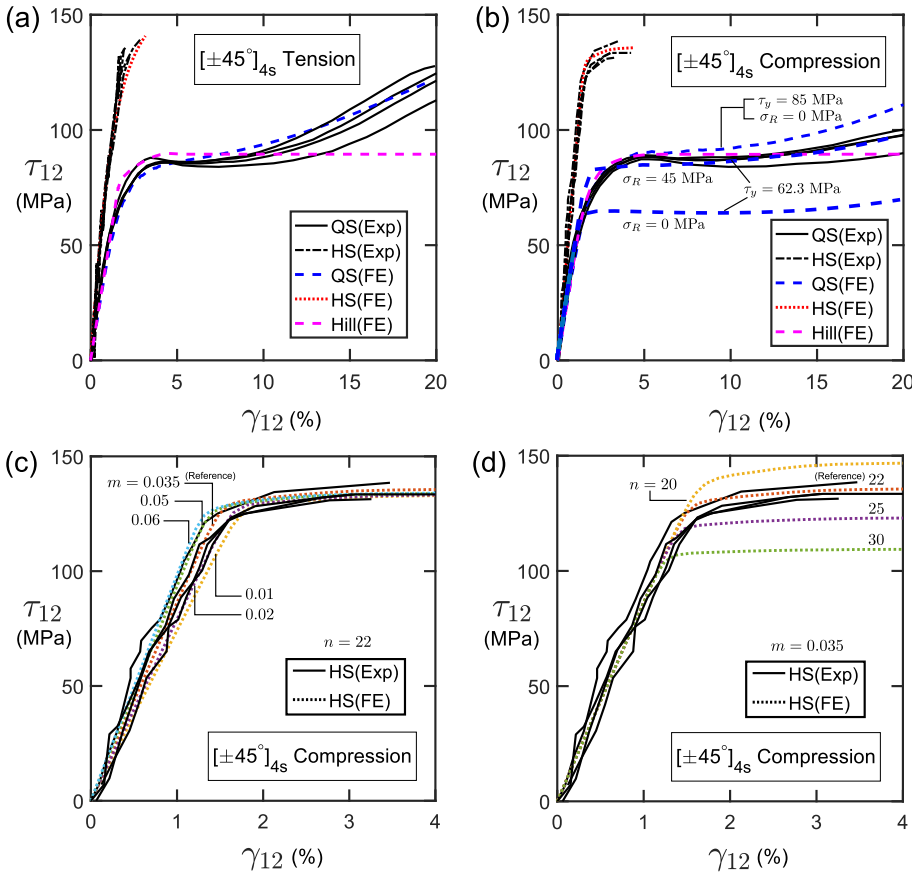


Fig. 12. Measured [5] and predicted shear stress-strain curves for (a) tension and (b) compression tests of composite laminates $[\pm 45^\circ]_{4s}$ under quasi-static and high strain rate loading. Note that the predicted stress-strain curves based on Hill's yield criterion and crystal model considering the residual stress effect are also included. Sensitivity study of the effect of (c) modulus coefficient m and (d) strength coefficient n upon the mechanical behaviour of compression tests of composite laminates $[\pm 45^\circ]_{4s}$ subjected to high strain rate loading.

accuracy, it does not capture the observed strain hardening behaviour, only predicting a perfectly-plastic response. The model predictions from our 'crystal model' are in a very good agreement with the measured responses for both strain rates. In particular, the model is able to account for the fibre rotation and reproduces the initial yield and linear hardening region for the tensile tests accurately, see Fig. 12a.

The hardening modulus in the compression simulation, as shown in Fig. 12b, is slightly higher than experiment, since the model does not consider the degradation of material properties due to matrix cracking and delamination [5]. Continuum damage models such as the combined plastic and smeared crack model [13,20,21] or the continuum shear damage models [1,62,63] have successfully captured the damage initiation and evolution in the composite laminates. Incorporating

continuum damage model with crystal plasticity model is beyond the scope of the present study and will be addressed in forthcoming studies.

4.6. Deformation mechanisms

After validating our model quantitatively against the measured stress-strain curves, we then proceed to reveal the deformation mechanisms in the $[\pm 45^\circ]_{4s}$ composite laminates under off-axis loading via FE predictions. The predicted local shear strain rate, shear strain and magnitude of fibre rotation under tensile and compressive loading were plotted in Fig. 13 and Fig. 14 respectively.

Although the measured strain contours and fibre rotation of $[\pm 45^\circ]_{4s}$ composite laminates under tensile and compressive loading are not

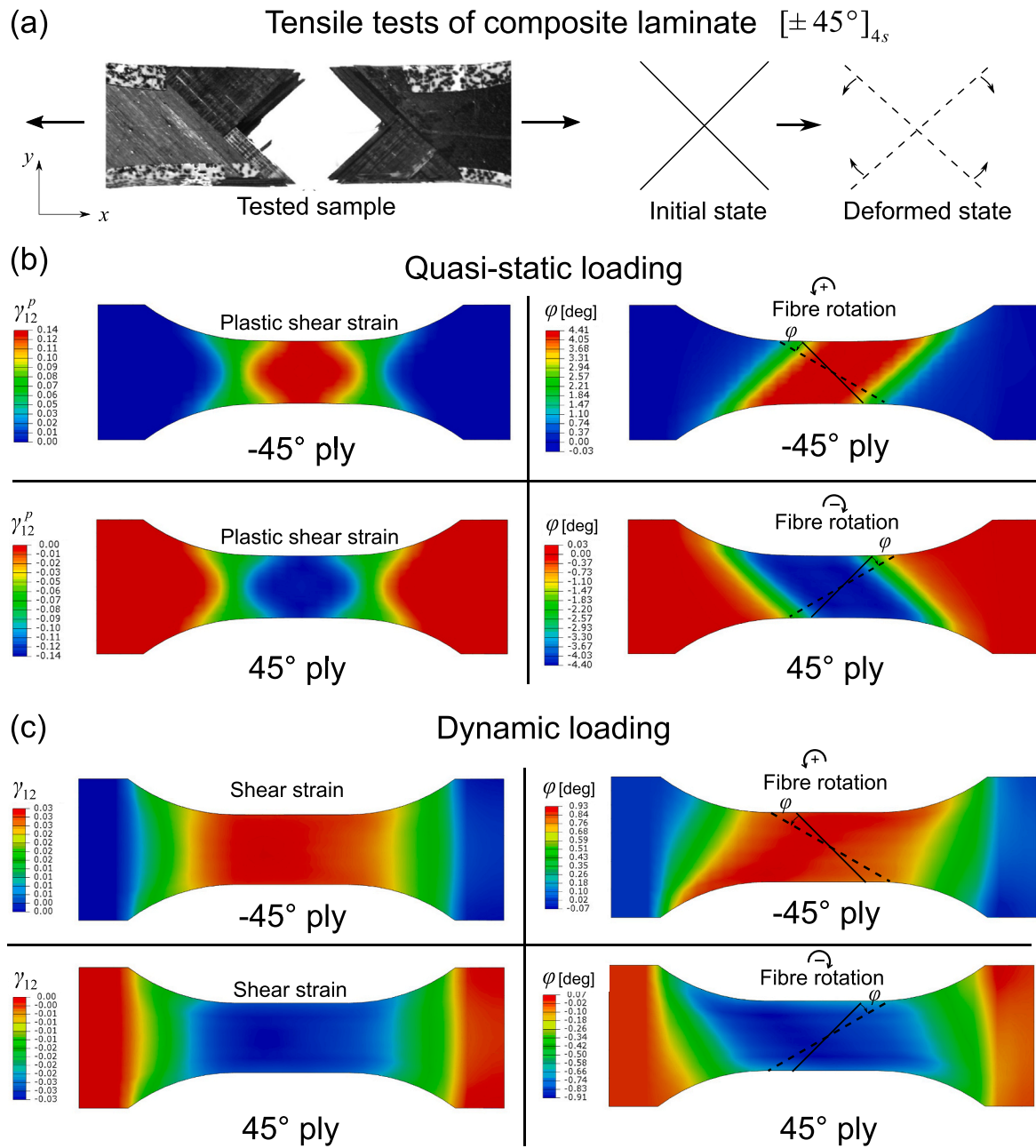


Fig. 13. (a) Composite laminates $[\pm 45^\circ]_{4s}$ after tensile test [5], predicted shear strain and fibre rotation contours under (b) quasi-static loading at a shear strain $\gamma = 15\%$ and (c) dynamic loading at a shear strain $\gamma = 4\%$. Note that the plastic shear strain in dynamic tensile tests is zero, hence only total shear strain is given.

available, the failed sample after dynamic tensile test shown in Fig. 13a gives an indication of the failure mode. The final angle between adjacent plies decreases compared to that of the initial state due to fibre rotation towards the loading direction. The matrix shear failure between individual fibres is the dominant failure mode, as suggested from the scanning electron microscopic images of fracture surfaces [5]. FE predicted strain contours are presented to reveal the internal plastic strain and fibre rotation. Predicted plastic shear strain contours in adjacent $\pm 45^\circ$ plies under quasi-static are plotted in Fig. 13b. All the plastic shear strain fields of $\pm 45^\circ$ plies with symmetric pattern indicate the interaction between adjacent plies. The shear stress in the 45° ply leads to in-plane plastic shear flow transverse to the fibre direction; this shear flow is resisted by the stiff fibres in the adjacent -45° ply. The resistance of this shear flow builds up a complementary shear stress in the adjacent plies, hence leading to a symmetric pattern in Fig. 13. This is different from the UD composite, where only a uniform shear band along the fibre

direction was developed, see Fig. 9b. In contrast, only elastic strain is observed in $\pm 45^\circ$ plies under dynamic loading, see Fig. 13c. The elastic shear strain under dynamic loading is distributed uniformly across the gauge section, indicating a linear-elastic response of material. This is consistent with the linear-elastic stress strain curve shown in Fig. 12a.

The rotation bands shown in Fig. 13b and c resemble the fibre scissoring phenomenon in the experiments [7] and provides quantitative evaluation of the fibre rotation ($\phi = 4.40^\circ - 4.76^\circ$). Recall that fibre rotation is only affected by the shear perpendicular to fibre orientation, the fibre rotation contours in Fig. 13 again show bands transverse to fibre directions. These fibre rotation bands have been revealed using X-ray computer tomography in tensile tests of $[\pm 45^\circ]_{2s}$ laminates by Sket et al. [6].

Fig. 14a demonstrates the failed sample after dynamic compressive test, where the final angle between neighbouring plies increases compared to that of initial state due to fibre rotation away from the

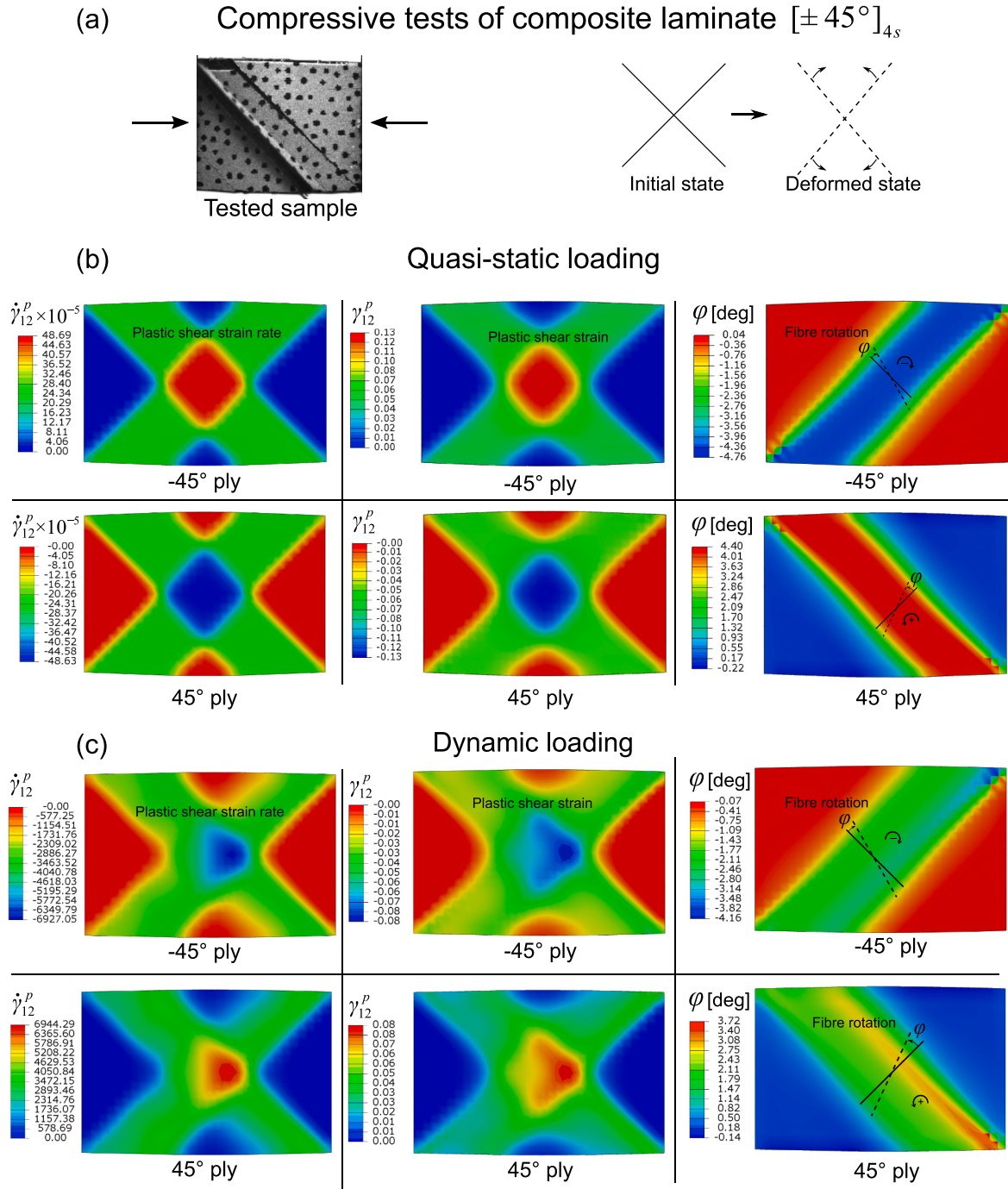


Fig. 14. (a) Composite laminates $[\pm 45^\circ]_{4s}$ after compressive test [5], predicted plastic shear strain rate, plastic shear strain and fibre rotation contours under (b) quasi-static loading at a shear strain $\gamma = 15\%$ and (c) dynamic loading at a shear strain $\gamma = 4\%$. Note that anticlockwise direction is defined as positive for fibre rotation.

loading direction. The predicted plastic shear rate contours and corresponding strain contours of $\pm 45^\circ$ plies under quasi-static and dynamic loading in Fig. 14b and c indicate the largest shear strain is located at the central region of the specimen. Two shear bands across each other are observed due to the complementary shear stress developed in the adjacent plies. In the dynamic test, due to the non-uniform local plastic strain rate distribution, the shear strain contour is also non-uniform. Fibre rotation bands transverse to fibre orientation are also exhibited in the compressive tests, see Fig. 14b and c, compare favourably to the fibre rotation observed in the failed sample.

5. Discussions

5.1. The effect of residual stress on the shear yield strength

It is noted that the shear yield strength used in our finite element simulations are different for UD laminates ($\tau_y = 62.3$ MPa) and CP laminates ($\tau_y = 85$ MPa). The hypothesis here is to associate the higher shear yield strength with a higher residual hydrostatic pressure generated during the curing and cooling of CP composite laminates. In order to verify this hypothesis, we proceed to introduce a residual stress in our finite element model. An average residual stress developed during the

Table 5

Computational cost of the crystal plasticity models and Hashin damage model for all the virtual tests in this study.

Sample	Strain rate (s^{-1})	Number of elements	Hashin model (mins)	Crystal model (mins)	Increase of computational cost (%)
UD-HS-Comp-45	331	6400	2.5	2.6	3
CP-HS-Comp	1300	2560	5.9	8.9	49
CP-HS-Tension	1300	19840	28.0	38.8	39
UD-QS-Comp-45	4×10^{-4}	6400	52.4	54.9	5
CP-QS-Comp	5×10^{-4}	2560	560.6	725.6	29
CP-QS-Tension	5×10^{-4}	19840	4677.7	5800.3	24

cure of CP composite laminates, measured by Cowley and Beaumont [64], is around $\sigma_R = 45$ MPa. This residual stress is introduced by applying a hydrostatic pressure of 45 MPa on all exterior surfaces of the CP composite laminates, similar with the method used in section 4.3.3. We demonstrate the effect of residual stress on the shear yield strength by modelling the compressive test of CP laminates. In these simulations, the shear yield strength is 62.3 MPa, the same value as used in UD laminates. As shown in Fig. 12 (b), the predicted yield strength increases to 83 MPa when accounting for a residual stress of 45 MPa, which is very close to the shear yield strength of composite laminates measured in the literature [5]. This analysis suggests the higher shear yield strength in the CP laminates could be attributed to a higher residual hydrostatic pressure generated during the curing and cooling of CP laminates.

5.2. Sensitivity study of the strain rate coefficients

The sensitivity study of the strain rate coefficients m and n on the mechanical behaviour of composite laminates $[\pm 45^\circ]_{4s}$ under high strain rate compressive loading is presented in this study. Since modulus coefficient m and strength coefficient n characterise the strain rate dependency of composite materials, their effect on stress-strain responses is negligible under quasi-static loading condition. Fig. 12c illustrates stress-strain curves when the modulus coefficient m varies from 0.01 to 0.06. The modulus of the predicted curve increases with the increasing m . A 500% increase of m only results in a 40% higher modulus, which means the material model is not very sensitive to the parameter of m . This justifies that even though there is a scatter in the measured material data for the modulus of different strain rates, it will have limited effect on the predictive capability of this model.

The effect of n on the stress-strain responses is shown in Fig. 12d. The yield strength increases with the decreasing n . A 36% increase of n gives rise to a 16% reduction of yield strength. This again confirms the material model is mildly sensitive to the choice of n , especially when n is larger than 20. Nevertheless, an accurate characterisation of the strain rate dependency of yield strength is still desirable for a good predictive capability of the high-fidelity finite element modelling.

5.3. Computational cost

The computational costs of the crystal plasticity model and Hashin damage model have been compared in Table 5. The computational cost of the crystal model is slightly higher than that of Hashin damage model. This is partially due to the 3D solid elements used by the crystal model, which are more computational expensive than continuum shell elements. Excluding the effect of element types, their computational costs would be relatively close. Nevertheless, it should be emphasised that the material is assumed linearly-elastic in the ABAQUS built-in Hashin damage model. Therefore, it is not able to capture the non-linear shear dominated plastic deformation. Additionally, the constitutive model

defined in the Hashin damage model is not capable to model the strain rate dependency.

6. Concluding remarks

A physically-based constitutive model was developed to predict the shear-dominated behaviour of composite laminates under finite deformation at different strain rates. The large plastic matrix shear deformation and associated fibre rotations were captured through framework based on crystal plasticity model.

Analytical models suggest the geometrical hardening behaviour of composite lamina is dependent on the longitudinal modulus and shear strain, whilst transverse compressive response of composite lamina is governed by the matrix shear yield strength and slip directions. Finite element simulations of uniaxial compression on UD composite and tensile/compressive tests of $[\pm 45^\circ]_{4s}$ composite laminates were conducted to validate this physically-based constitutive model. The strain rate dependency of the material is found to be dominated by the local plastic shear strain rate. Good qualitative and quantitative correlations were achieved between the numerical models and experimental results. The fidelity of the computational models was also able to provide detailed information on the plastic shear strain, fibre rotation, strain rate effect, hydrostatic pressure dependency and residual stress effect.

Future work will focus on incorporating continuum damage mechanics to capture the evolution of matrix cracking and fibre-dominated breakage in the development of pseudo-ductile [65], damage-tolerant [66] and crashworthy [67,68] carbon fibre composites including a large amount non-linear shear failure. This crystal plasticity model can be also extended to model the non-linear deformation of carbon nanotube mats and related composites, as studies suggest the non-linear deformation is dominated by the longitudinal shear deformation of CNT bundles [69,70].

CRediT authorship contribution statement

Wei Tan: Conceptualization, Formal analysis, Funding acquisition, Investigation, Methodology, Software, Validation, Visualization, Writing - original draft. **Burigede Liu:** Methodology, Software, Writing - review & editing.

Acknowledgement

W. Tan would like to gratefully acknowledge the start-up funding from Queen Mary University of London (SEM9241) and CAPE Acorn Cambridge Blue Sky Research Award (NMZG/256). W. Tan thanks Prof. Norman A. Fleck and Prof. Brian G. Falzon for some useful discussions and suggestions on this work. B.G. Liu is grateful for Prof. Vikram Deshpande for many inspiring discussions on this work.

Appendix A. Algorithm for the constitutive model

The algorithm for the implementation of the physically-based model is presented below and is repeated until the end of the time increment.

- (1) Collect total deformation gradients F_{ij} and stretch tensors U_{ij} from ABAQUS VUMAT.
- (2) In the initial elastic regime, $F_{ij}^e = F_{ij}$, calculate elastic Green-Lagrange strains $E_{ij}^e = \frac{1}{2}(F_{ki}^e F_{kj}^e - \delta_{ij})$, see Eq. (9).
- (3) Material stresses $\Sigma_{ij} = C_{ijkl} E_{kl}^e$, see Eq. (10) for the detail.
- (4) Update Cauchy stresses $\sigma_{ij} = [\det(F_{ij}^e)]^{-1} F_{ik}^e \Sigma_{kl} F_{jl}^e$, see Eq. (11).
- (5) Initialise the plastic deformation gradient tensors F_{ij}^p , start from zero.
- (6) Resolved shear stresses $\tau^{(\alpha)} = s_i^{*(\alpha)} \sigma_{ij} m_j^{*(\alpha)}$, Eq. (13)
- (7) Pressure-dependent resolved shear stresses $\tau^{(\alpha)} = \tau_y + \mu P$, see Eq. (14)
- (8) Rate-dependency shear strain rates $\dot{\gamma} = \dot{\gamma}_0 \left(\frac{\tau^{(\alpha)}}{\tau_y} \right)^n \text{sgn}(\tau^{(\alpha)})$, see Eq. (12)
- (9) Plastic velocity gradient rates $L_{ij}^p = \sum_{\alpha} \dot{\gamma}^{(\alpha)} s_i^{*(\alpha)} m_j^{*(\alpha)}$, see Eq. (3).
- (10) The plastic deformation gradient is calculated using $F_{ij}^{p, t+\Delta t} = \dot{F}_{ij}^p \Delta t + F_{ij}^{p, t}$, see Eq. (4).
- (11) The total deformation gradient in the new time step is calculated as $F_{ij} = F_{ij}^e F_{ij}^p$, see Eq. (1).
- (12) Update the slip systems $s_i^{*(\alpha)} = F_{ij}^e s_i^{*(\alpha)}$ and $m_i^{*(\alpha)} = m_i^{*(\alpha)} (F_{ij}^e)^{-1}$, see Eq. (5) and Eq. (6).
- (13) Go back to step (1)

Appendix B. Analytical model for simple shear

Consider a two-dimensional plain strain single element subjected to simple shear perpendicular to fibre direction, as shown in Fig. 5, the total shear strain is defined as $\gamma = \tan(\omega)$, where it can be decomposed into elastic strain γ_e and plastic strain γ_p as follows,

$$\gamma = \gamma_e + \gamma_p \quad (\text{B1})$$

The total deformation gradient is given by,

$$F_{ij} = \begin{bmatrix} 1 & 0 \\ \gamma & 1 \end{bmatrix} \quad (\text{B2})$$

where it is decomposed into elastic deformation gradient F_{ij}^e ,

$$F_{ij}^e = \begin{bmatrix} 1 & -\gamma_p \\ \gamma & 1 - \gamma_p \gamma \end{bmatrix} \quad (\text{B3})$$

and plastic deformation gradient F_{ij}^p , see Fig. 2.

$$F_{ij}^p = \begin{bmatrix} 1 & \gamma_p \\ 0 & 1 \end{bmatrix}. \quad (\text{B4})$$

The Green strain E_{ij} is given by,

$$E_{ij} = \frac{1}{2} (F_{ki}^e F_{kj}^e - \delta_{ij}) = \frac{1}{2} \begin{bmatrix} \gamma^2 & \gamma - \gamma_p - \gamma_p \gamma^2 \\ \gamma - \gamma_p - \gamma_p \gamma^2 & \gamma_p^2 + \gamma_p^2 \gamma^2 - 2\gamma_p \gamma \end{bmatrix} \quad (\text{B5})$$

Omit the high-order term $O(t^3)$ and $O(t^4)$, the Green strain E_{ij} is simplified into,

$$E_{ij} = \frac{1}{2} \begin{bmatrix} \gamma^2 & \gamma_e \\ \gamma_e & \gamma_p^2 - 2\gamma_p \gamma \end{bmatrix}. \quad (\text{B6})$$

The second Piola-Kirchhoff stress (PK2) is calculated from $\Sigma_{ij} = C_{ijkl} E_{kl}$, in Voigt notation,

$$\Sigma_{ij} = C_{ijkl} E_{kl} = \begin{pmatrix} \frac{E_f}{(1 - \nu_{12}\nu_{21})} (E_{11} + \nu_{21} E_{22}) \\ \frac{E_m}{(1 - \nu_{12}\nu_{21})} (\nu_{12} E_{11} + E_{22}) \\ 2G_{12} E_{12} \end{pmatrix} \quad (\text{B7})$$

Substitute the PK2 stress into the equation $\sigma_{ij} = [\det(F_{ij}^e)]^{-1} F_{ki}^e \Sigma_{kl} F_{jl}^e$, we obtain the shear stress is given by,

$$\tau_{12} = (\Sigma_{11} - \gamma_p \Sigma_{12}) \gamma + (\Sigma_{12} - \gamma_p \Sigma_{22}) (1 - \gamma_p \gamma). \quad (\text{B8})$$

Substitute Σ_{11} , Σ_{12} and Σ_{22} into Eq. (B8) and omit the high-order terms, we have the final formula as follow,

$$\tau_{12} = \begin{cases} G_{12} \gamma & \gamma_p = 0 \\ \tau_y + 0.5 (E_f \gamma^3 - E_m \gamma_p^3) & \gamma_p > 0 \end{cases} \quad (\text{B9})$$

Since $E_f \gg E_m$, Eq. (B9) can be further simplified as,

$$\tau_{12} = \begin{cases} G_{12}\gamma & \gamma_p = 0 \\ \tau_y + 0.5E_f\gamma^3 & \gamma_p > 0 \end{cases} \quad (\text{B10})$$

This equation indicates the shear stress developed in the simple shear-90° (shear perpendicular to fibre direction) is directly related to longitudinal and transverse modulus.

Following the same approach, we derive the analytical solution for the simple shearing parallel to fibre direction. The final equation is given by,

$$\tau_{12} = \begin{cases} G_{12}\gamma & \gamma_p = 0 \\ \tau_y & \gamma_p > 0 \end{cases} \quad (\text{B11})$$

Appendix C. Analytical model for transverse compression

Consider the transverse compression on the unidirectional composite lamina, see Fig. A1. Assume the slip direction (dash line) oriented at the angle of θ with respect to the loading direction. The slip angle β defined in the crystal plasticity model is the angle between slip direction and a perpendicular plane to the loading axis.

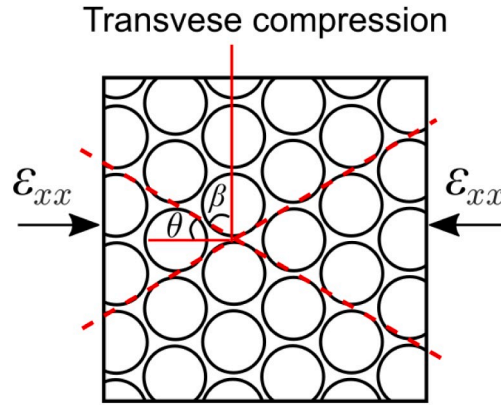


Fig. A1. The angles in the transverse compressive loading on UD composite.

The global stress (x-y-z coordinate system) and the local stress (1-2-3 coordinate system) developed in the slip plane is related via standard transformation matrix below,

$$\begin{Bmatrix} \sigma_2 \\ \sigma_3 \\ \tau_{23} \end{Bmatrix} = \begin{bmatrix} m^2 & n^2 & 2mn \\ n^2 & m^2 & -2mn \\ -mn & mn & (m^2 - n^2) \end{bmatrix} \begin{Bmatrix} \sigma_y \\ \sigma_z \\ \tau_{yz} \end{Bmatrix} \quad (\text{C1})$$

Where $m = \cos \theta$, $n = \sin \theta$.

In the uniaxial compression case, $\sigma_y = 0$ and $\tau_{yz} = 0$. Therefore, the local shear stress developed in the slip plane is given by,

$$\tau_{23} = -\cos \theta \sin \theta \sigma_y = -\frac{1}{2} \sin 2\theta \sigma_y \quad (\text{C2})$$

Slip occurs when the shear stress arising from the external loading exceeds a critical resolved shear stress $\tau^{(a)}$, see Eq. (14). Here we set $\tau_{23} = \tau^{(a)}$, including the pressure-dependency. Since the $\theta = 90^\circ - \beta$, the transverse yield strength σ_y follows immediately as,

$$\sigma_y = \frac{2\tau^{(a)}}{\sin 2\beta} \quad (\text{C3})$$

References

- [1] Tan W, Falzon BG. Modelling the nonlinear behaviour and fracture process of AS4/PEKK thermoplastic composite under shear loading. *Compos Sci Technol* 2016;126: 60–77. <https://doi.org/10.1016/j.compscitech.2016.02.008>.
- [2] Czél G, Wisnom MR. Demonstration of pseudo-ductility in high performance glass/epoxy composites by hybridisation with thin-ply carbon prepreg. *Compos. Part A Appl Sci Manuf* 2013;52:23–30. <https://doi.org/10.1016/j.COMPOSITESA.2013.04.006>.
- [3] Kolanu NR, Raju G, Ramji M. Damage assessment studies in CFRP composite laminate with cut-out subjected to in-plane shear loading. *Compos B Eng* 2019;166: 257–71. <https://doi.org/10.1016/j.compositesb.2018.11.142>.
- [4] Koerber H, Xavier J, Camanho PP. High strain rate characterisation of unidirectional carbon-epoxy IM7-8552 in transverse compression and in-plane shear using digital image correlation. *Mech Mater* 2010;42:1004–19. <https://doi.org/10.1016/j.mechmat.2010.09.003>.
- [5] Cui H, Thomson D, Pellegrino A, Wiegand J, Petrinic N. Effect of strain rate and fibre rotation on the in-plane shear response of $\pm 45^\circ$ laminates in tension and compression tests. *Compos Sci Technol* 2016;135:106–15. <https://doi.org/10.1016/j.compscitech.2016.09.016>.
- [6] Sket F, Enfedaque A, Alton C, González C, Molina-Aldareguia JM, Llorca J. Automatic quantification of matrix cracking and fiber rotation by X-ray computed tomography in shear-deformed carbon fiber-reinforced laminates. *Compos Sci Technol* 2014;90:129–38. <https://doi.org/10.1016/j.compscitech.2013.10.022>.
- [7] Wisnom MR. The effect of fibre rotation in $\pm 45^\circ$ tension tests on measured shear properties. *Composites* 1995;26:25–32. [https://doi.org/10.1016/0010-4361\(94\)P3626-C](https://doi.org/10.1016/0010-4361(94)P3626-C).
- [8] Totry E, Molina-Aldareguia JM, González C, Llorca J. Effect of fiber, matrix and interface properties on the in-plane shear deformation of carbon-fiber reinforced composites. *Compos Sci Technol* 2010;70:970–80. <https://doi.org/10.1016/j.compscitech.2010.02.014>.

- [9] Hashin Z. On elastic behaviour of fibre reinforced materials of arbitrary transverse phase geometry. *J Mech Phys Solid* 1965;13:119–34. [https://doi.org/10.1016/0022-5096\(65\)90015-3](https://doi.org/10.1016/0022-5096(65)90015-3).
- [10] Puck A, Schürmann H. Failure analysis of FRP laminates by means of physically based phenomenological models. *Compos Sci Technol* 2002;62:1633–62. [https://doi.org/10.1016/S0266-3538\(01\)00208-1](https://doi.org/10.1016/S0266-3538(01)00208-1).
- [11] Pinho ST, Iannucci L, Robinson P. Physically-based failure models and criteria for laminated fibre-reinforced composites with emphasis on fibre kinking: Part I: Development. *Compos. Part A Appl Sci Manuf* 2006;37:63–73. <https://doi.org/10.1016/J.COMPOSITESA.2005.04.016>.
- [12] Tan W, Falzon BG, Chiu LNS, Price M. Predicting low velocity impact damage and Compression-After-Impact (CAI) behaviour of composite laminates. *Compos. Part A Appl Sci Manuf* 2015;71:212–26. <https://doi.org/10.1016/j.compositesa.2015.01.025>.
- [13] Camanho PP, Bessa MA, Catalanotti G, Vogler M, Rolfes R. Modeling the inelastic deformation and fracture of polymer composites – Part II: smeared crack model. *Mech Mater* 2013;59:36–49. <https://doi.org/10.1016/J.MECHMAT.2012.12.001>.
- [14] Catalanotti G, Camanho PP, Marques AT. Three-dimensional failure criteria for fiber-reinforced laminates. *Compos Struct* 2013;95:63–79. <https://doi.org/10.1016/J.COMPSTRUCT.2012.07.016>.
- [15] Sabik A. Direct shear stress vs strain relation for fiber reinforced composites. *Compos B Eng* 2018;139:24–30. <https://doi.org/10.1016/j.compositesb.2017.11.057>.
- [16] Liu H, Liu J, Ding Y, Zhou J, Kong X, Harper LT, Blackman BRK, Falzon BG, Dear JP. Modelling damage in fibre-reinforced thermoplastic composite laminates subjected to three-point bend loading. *Compos Struct* 2020;236:111889. <https://doi.org/10.1016/j.compstruct.2020.111889>.
- [17] Sun CT, Zhu C. The effect of deformation-induced change of fiber orientation on the non-linear behavior of polymeric composite laminates. *Compos Sci Technol* 2000;60:2337–45. [https://doi.org/10.1016/S0266-3538\(00\)00029-4](https://doi.org/10.1016/S0266-3538(00)00029-4).
- [18] Maugot BR, Minnetyan L, Chamis CC. Large deformation nonlinear response of soft composite structures via laminate analogy. *J Adv Mater* 2001;34:21–6.
- [19] Mandel U, Taubert R, Hinterhölzl R. Three-dimensional nonlinear constitutive model for composites. *Compos Struct* 2016;142:78–86. <https://doi.org/10.1016/J.COMPSTRUCT.2016.01.080>.
- [20] Vogler M, Rolfes R, Camanho PP. Modeling the inelastic deformation and fracture of polymer composites – Part I: plasticity model. *Mech Mater* 2013;59:50–64. <https://doi.org/10.1016/J.MECHMAT.2012.12.002>.
- [21] Koerber H, Camanho PP. High strain rate characterisation of unidirectional carbon-epoxy IM7-8552 in longitudinal compression. *Compos. Part A* 2011;42:462–70. <https://doi.org/10.1016/j.compositesa.2011.01.002>.
- [22] Laux T, Gan KW, Dulieu-Barton JM, Thomsen OT. A simple nonlinear constitutive model based on non-associative plasticity for UD composites: development and calibration using a Modified Arcan Fixture. *Int J Solid Struct* 2019;162:135–47. <https://doi.org/10.1016/J.IJSTR.2018.12.004>.
- [23] Hill R. A theory of the yielding and plastic flow of anisotropic metals. *Proc. R. Soc. A Math. Phys. Eng. Sci.* 1948;193:281–97. <https://doi.org/10.1098/rspa.1948.0045>.
- [24] Dafalias YF. The plastic spin concept and a simple illustration of its role in finite plastic transformations. *Mech Mater* 1984;3:223–33. [https://doi.org/10.1016/0167-6636\(84\)90021-8](https://doi.org/10.1016/0167-6636(84)90021-8).
- [25] Aravas N. Finite-strain anisotropic plasticity and the plastic spin. *Model Simulat Mater Sci Eng* 1994;2:483–504. <https://doi.org/10.1088/0965-0393/2/3A/005>.
- [26] Eskandari S, Andrade Pires FM, Camanho PP, Marques AT. Intralaminar damage in polymer composites in the presence of finite fiber rotation: Part I- Constitutive model. *Compos Struct* 2016;151:114–26. <https://doi.org/10.1016/j.compstruct.2016.01.047>.
- [27] Hill R, Rice JR. Constitutive analysis of elastic-plastic crystals at arbitrary strain. *J Mech Phys Solid* 1972;20:401–13. [https://doi.org/10.1016/0022-5096\(72\)90017-8](https://doi.org/10.1016/0022-5096(72)90017-8).
- [28] Asaro RJ. Micromechanics of crystals and polycrystals. *Adv Appl Mech* 1983;23:1–115. [https://doi.org/10.1016/S0065-2156\(08\)70242-4](https://doi.org/10.1016/S0065-2156(08)70242-4).
- [29] Liu BG, Kandan K, Wadley HNG, Deshpande VS. Deep penetration of ultra-high molecular weight polyethylene composites by a sharp-tipped punch. *J Mech Phys Solid* 2019;123:80–102. <https://doi.org/10.1016/J.JMPS.2018.06.001>.
- [30] Liu BG, Kandan K, Wadley HNG, Deshpande VS. High strain rate compressive response of ultra-high molecular weight polyethylene fibre composites. *Int J Plast* 2019. <https://doi.org/10.1016/j.ijplas.2019.04.005>.
- [31] Liu BG, Wadley HNG, Deshpande VS. Failure mechanism maps for ultra-high molecular weight polyethylene fibre composite beams impacted by blunt projectiles. *Int J Solid Struct* 2019;178–179:180–98. <https://doi.org/10.1016/j.ijlstr.2019.07.001>.
- [32] Meza Lucas R, Schormans Jim MJ, Remmers oris JC, Deshpande Vikram S. Shear response of 3D non-woven carbon fibre reinforced composites. *J. Mech. Phys. Solid.* 2019;125:276–97.
- [33] Daniel IM, Werner BT, Fenner JS. Strain-rate-dependent failure criteria for composites. *Compos Sci Technol* 2011;71:357–64. <https://doi.org/10.1016/J.COMPSCITECH.2010.11.028>.
- [34] Sorini C, Chattopadhyay A, Goldberg RK. An improved plastically dilatant unified viscoplastic constitutive formulation for multiscale analysis of polymer matrix composites under high strain rate loading. *Compos B Eng* 2020;184. <https://doi.org/10.1016/j.compositesb.2019.107669>.
- [35] Wang J, Wen L, Xiao J, Liang T, Hu X, Li P. The mechanical properties and constitutive model of two woven composites including the influences of temperature, strain rate and damage growth. *Compos B Eng* 2019;161:502–13. <https://doi.org/10.1016/j.compositesb.2018.12.137>.
- [36] Liu H, Falzon BG, Tan W. Experimental and numerical studies on the impact response of damage-tolerant hybrid unidirectional/woven carbon-fibre reinforced composite laminates. *Compos B Eng* 2018;136:101–18. <https://doi.org/10.1016/j.compositesb.2017.10.016>.
- [37] Liu H, Falzon BG, Tan W. Predicting the Compression-After-Impact (CAI) strength of damage-tolerant hybrid unidirectional/woven carbon-fibre reinforced composite laminates. *Compos. Part A Appl Sci Manuf* 2018;105:189–202. <https://doi.org/10.1016/j.compositesa.2017.11.021>.
- [38] Cui H, Thomson D, Pellegrino A, Wiegand J, Petrinic N. Effect of strain rate and fibre rotation on the in-plane shear response of $\pm 45^\circ$ laminates in tension and compression tests. *Compos Sci Technol* 2016;135:106–15. <https://doi.org/10.1016/j.compscitech.2016.09.016>.
- [39] Schaefer JD, Werner BT, Daniel IM. Strain-rate-dependent failure of a toughened matrix composite. *Exp Mech* 2014;54:1111–20. <https://doi.org/10.1007/s11340-014-9876-0>.
- [40] Koerber H, Kuhn P, Ploekl M, Otero F, Gerbaud P-W, Rolfes R, Camanho PP. Experimental characterization and constitutive modeling of the non-linear stress-strain behavior of unidirectional carbon-epoxy under high strain rate loading. *Adv. Model. Simul. Eng. Sci.* 2018;5:17. <https://doi.org/10.1186/s40323-018-0111-x>.
- [41] González C, Llorca J. Mechanical behavior of unidirectional fiber-reinforced polymers under transverse compression: microscopic mechanisms and modeling. *Compos Sci Technol* 2007;67:2795–806. <https://doi.org/10.1016/j.compscitech.2007.02.001>.
- [42] Tan W, Naya F, Yang L, Chang T, Falzon BG, Zhan L, Molina-Aldareguía JM, González C, Llorca J. The role of interfacial properties on the intralaminar and interlaminar damage behaviour of unidirectional composite laminates: experimental characterization and multiscale modelling. *Compos B Eng* 2017;138:206–21. <https://doi.org/10.1016/j.compositesb.2017.11.043>.
- [43] Asaro RJ, Needleman A. Overview no. 42 Texture development and strain hardening in rate dependent polycrystals. *Acta Metall* 1985;33:923–53. [https://doi.org/10.1016/0001-6160\(85\)90188-9](https://doi.org/10.1016/0001-6160(85)90188-9).
- [44] Asaro RJ. Crystal plasticity. *J Appl Mech* 1983;50:921. <https://doi.org/10.1115/1.3167205>.
- [45] Partridge PG. The crystallography and deformation modes of hexagonal close-packed metals. *Metall Rev* 1967;12:169–94. <https://doi.org/10.1179/mtrl.1967.12.1.169>.
- [46] Barlat F, Lege DJ, Brem JC. A six-component yield function for anisotropic materials. *Int J Plast* 1991;7:693–712. [https://doi.org/10.1016/0749-6419\(91\)90052-Z](https://doi.org/10.1016/0749-6419(91)90052-Z).
- [47] Puck A, Schürmann H. Failure analysis of FRP laminates by means of physically based phenomenological models. *Compos Sci Technol* 1998;58:1045–67. [https://doi.org/10.1016/S0266-3538\(96\)00140-6](https://doi.org/10.1016/S0266-3538(96)00140-6).
- [48] Paul B. A modification of the coulomb-mohr theory of fracture. *J. Appl. Mech. Trans. ASME.* 1960;28:259–68. <https://doi.org/10.1115/1.3641665>.
- [49] Davila CG, Camanho PP, Rose CA. Failure criteria for FRP laminates. *J Compos Mater* 2005;39:323–45. <https://doi.org/10.1177/0021998305046452>.
- [50] Naya F, González C, Lopes CS, Van Der Veen S, Pons F. Computational micromechanics of the transverse and shear behavior of unidirectional fiber reinforced polymers including environmental effects. 2017. <https://doi.org/10.1016/j.compositesa.2016.06.018>.
- [51] Chang T, Zhan L, Tan W. Void content and interfacial properties of composite laminates under different autoclave cure pressure. *Compos Interfac* 2017;24:529–40. <https://doi.org/10.1080/09276440.2016.1237113>.
- [52] Spitzig Wa, Richmond O. Effect of hydrostatic pressure on the deformation behavior of polyethylene and polycarbonate in tension and in compression. *Polym Eng Sci* 1979;19:1129–39. <https://doi.org/10.1002/pen.760191602>.
- [53] Pae KD, Rhee KY. Effects of hydrostatic pressure on the compressive behavior of thick laminated 45° and 90° unidirectional graphite-fiber/epoxy-matrix composites. *Compos Sci Technol* 1995;53:281–7. [https://doi.org/10.1016/0266-3538\(94\)00080-8](https://doi.org/10.1016/0266-3538(94)00080-8).
- [54] Hashin Z. Failure criteria for unidirectional fiber composites. *J. Appl. Mech. Trans. ASME.* 1980;47:329–34. <https://doi.org/10.1115/1.3153664>.
- [55] Simulia DS. Abaqus 6.14, abaqus 6.14 anal. User's Guid.; 2014.
- [56] Melin LN, Neumeister JM. Measuring constitutive shear behavior of orthotropic composites and evaluation of the modified Iosipescu test. *Compos Struct* 2006;76:106–15. <https://doi.org/10.1016/j.compstruct.2006.06.016>.
- [57] Budiansky B, Fleck NA. Compressive failure of fibre composites. *J Mech Phys Solid* 1993;41:183–211. [https://doi.org/10.1016/0022-5096\(93\)90068-Q](https://doi.org/10.1016/0022-5096(93)90068-Q).
- [58] Sassi S, Tarfaoui M, Nachtane M, Ben Yahia H. Strain rate effects on the dynamic compressive response and the failure behavior of polyester matrix. *Compos B Eng* 2019;174. <https://doi.org/10.1016/j.compositesb.2019.107040>.
- [59] Chen C, Zhang C, Liu C, Miao Y, Wong SC, Li Y. Rate-dependent tensile failure behavior of short fiber reinforced PEEK. *Compos B Eng* 2018;136:187–96. <https://doi.org/10.1016/j.compositesb.2017.10.031>.
- [60] Kim DH, Kang SY, Kim HJ, Kim HS. Strain rate dependent mechanical behavior of glass fiber reinforced polypropylene composites and its effect on the performance of automotive bumper beam structure. *Compos B Eng* 2019;166:483–96. <https://doi.org/10.1016/j.compositesb.2019.02.053>.
- [61] Fan J, Wang C. Dynamic compressive response of a developed polymer composite at different strain rates. *Compos B Eng* 2018;152:96–101. <https://doi.org/10.1016/j.compositesb.2018.06.025>.
- [62] Tan W, Falzon BG, Price M, Liu H. The role of material characterisation in the crush modelling of thermoplastic composite structures. *Compos Struct* 2016;153:914–27. <https://doi.org/10.1016/j.compstruct.2016.07.011>.
- [63] Tan W, Falzon BG, Chiu LNS, Price M. Predicting low velocity impact damage and Compression-After-Impact (CAI) behaviour of composite laminates. *Compos. Part*

- A Appl Sci Manuf 2015;71:212–26. <https://doi.org/10.1016/j.compositesa.2015.01.025>.
- [64] Cowley KD, Beaumont PWR. The measurement and prediction of residual stresses in carbon-fibre/polymer composites. *Compos Sci Technol* 1997;57:1445–55. [https://doi.org/10.1016/S0266-3538\(97\)00048-1](https://doi.org/10.1016/S0266-3538(97)00048-1).
- [65] Fuller JD, Wisnom MR. Pseudo-ductility and damage suppression in thin ply CFRP angle-ply laminates. *Compos. Part A Appl Sci Manuf* 2015;69:64–71. <https://doi.org/10.1016/J.COMPOSITESA.2014.11.004>.
- [66] Li X, Ma D, Liu H, Tan W, Gong X, Zhang C, Li Y. Assessment of failure criteria and damage evolution methods for composite laminates under low-velocity impact. *Compos Struct* 2019;207:727–39. <https://doi.org/10.1016/j.compstruct.2018.09.093>.
- [67] Tan W, Falzon BG. Modelling the crush behaviour of thermoplastic composites. *Compos Sci Technol* 2016;134:57–71. <https://doi.org/10.1016/j.compscitech.2016.07.015>.
- [68] Falzon BG, Tan W. Virtual testing of composite structures: progress and challenges in predicting damage, residual strength and crashworthiness. In: *Struct. Integr. Carbon fiber compos*; 2016.
- [69] Stallard JC, Tan W, Smail FR, Gspann TS, Boies AM, Fleck NA. The mechanical and electrical properties of direct-spun carbon nanotube mats. *Extrem. Mech. Lett.* 2018;21:65–75. <https://doi.org/10.1016/J.EML.2018.03.003>.
- [70] Tan W, Stallard JC, Smail FR, Boies AM, Fleck NA. The mechanical and electrical properties of direct-spun carbon nanotube mat-epoxy composites. *Carbon N. Y.* 2019;150:489–504. <https://linkinghub.elsevier.com/retrieve/pii/S0008622319304610>.